A Spectroscopic Study of Fe Phases in Cemented Carbides

Mosse Ibwanga

March 2016

A dissertation submitted to the Faculty of Science, University of the

Witwatersrand, Johannesburg, in fulfilment of the academic requirements for the

Degree of Master of Science

Declaration

The measurements reported in this dissertation were carried out at the University of the Witwatersrand, Johannesburg, South Africa.

The data analysis and understanding of results is my own work and was carried under the guidance of Professor D. Naidoo (supervisor) and Dr H. Masenda (co-supervisor).

The work of other scientists is duly acknowledged when used in this dissertation.

This dissertation has not been submitted before for any degree or examination at any other University.

Mosse Ibwanga

Monday, 27th Jully 2016

Abstract

Tungsten carbide (WC) is characterized by its high strength, toughness, hardness, its high resistance to wear and can also be employed at high temperatures. It is used mainly in the form of cemented tungsten carbides which are produced by combining grains of tungsten carbide into a binder matrix element, for example cobalt (Co). Tungsten carbide is commonly used in industrial machinery as cutting tools and abrasives.

The primary aim of this project is to investigate the effects of iron (Fe) as an alternative/additional binder in a tungsten carbide system. Therefore, two samples WC-10wt%Co-6wt%TiC and WC-10wt%Co-6wt%TiC-20wt%Fe alloys were prepared by milling and followed by sintering. Several studies have been undertaken in this project to ascertain the effect of Fe on the structural, electronic, magnetic and physical properties of the as-milled and as-sintered samples. A number of different experimental methods were applied to give such information.

Transmission Mössbauer spectroscopy and conversion electron Mössbauer spectroscopy were employed as the main techniques to determine the charge states of Fe, Fe phases and other complex phases in the WC-10wt%Co-6wt%TiC-20wt%Fe alloy from the hyperfine interaction parameters. In addition, applied Vickers hardness test, scanning electron microscopy (SEM), energy dispersive X-ray spectroscopy (EDS), X-ray diffraction (XRD) and strain analysis were utilized as complementary characterization techniques.

The Vickers hardness value of 1358±70 HV was measured for the WC-Co-TiC sample whilst a lower value of 820±41 HV was found for the WC-Co-TiC-Fe sample. The microstructure analysis (SEM/EDS) confirmed the presence of WC in the matrix, and Co, Ti, and Fe as the binder elements. XRD results show the formation of the FeCo alloy in the as-milled powder and as-sintered samples. The strain analysis was performed on the as-milled powder, and the as-sintered samples by adopting the method used in accordance with the Topas description, defined in the Topas manual. The WC-Co-TiC sample showed that the tungsten carbide phase appears to have little strain whilst the titanium carbide phase appeared to have no

strain. In the WC-Co-TiC-Fe sample, all phases show no strain. The Mössbauer spectrum at room temperature acquired from transmission Mössbauer spectroscopy was fitted with one sextet S1 attributed to α-Fe. Best fits to the data obtained from conversion electron Mössbauer spectroscopy required four spectral components: two sextets S1 and S2 assigned to FeCo, one doublet D1 assigned to FeWC and one single SL1 assigned to FeTi alloy.

Acknowledgements

Firstly, I would like to thank God The Almighty (God of surprise) for everything that he has done in my life and all things he will be doing everywhere I shall be. Next, I am indebted to my supervisor Professor D. Naidoo and co-supervisor, Dr H. Masenda for enhancing my life in this research despite my previous qualification in science chemistry and their assistance during my experimental work, data analysis, for taking time to read through the drafts of this dissertation, I am grateful for their comments, suggestion, over all their encouragements and for time consuming consultations in spite of their commitments within the University. Many thanks!

I am grateful to Drs P. Oladijo, R. Genga, R. Warmbier and Mr. G. Peter for their invaluable expertise and their critical comments during the project. I would like to acknowledge the financial support provided by the Department of Science and Technology and the National Research Foundation Centre of Excellence in Strong Materials (DST-NRF CoE-SM), South Africa. In addition, I would like to thank Professor L. Cornish the director of the DST-NRF CoE-SM and all members of her team for their administrative assistance provided during my study. Thank you!

I wish to take this opportunity to express thanks to my family particularly to my wife Light Bopita, my lovely children Daniel and Believe Mosse. I would like to extend my gratitude to the following family members: Mosse, Bopita, Diantantu, Nkazi, Tandu, Mbiombi, Mufula, Kalala, Mwamba and my colleagues Adeleke, Nkosiphile, Ncube, Ross, Warren, Gerrard also my friends Makabu, Bokendo, Badibanga, Kalondji, Lobo, Mambu, Matindi and finally all my family and friends from abroad.

Finally, I am grateful to all Professors, Doctors and teaching assistants in the school of Physics, Faculty of Science and the university in general. This work would not have been possible without the assistance provided by my supervisors, families, colleagues and friends. Thank you so much!

As the rain and the snow come down from heaven, and do not return to it without watering the earth and making it bud and flourish, so that it yield seed for the sower and bread for the eater.

Isaiah 55:10

Table of Contents

List of Figures

List of Tables

Chapter 1

Introduction

Carbides made with transition metals have very high mechanical hardness, high temperature strength, and high melting point. In addition, these carbides are also good thermal and electrical conductors [1] compared to other alkali-like metals hence, have a wide range of industrial uses for example in metallurgy, electronics, and as catalysts. The transition metal compounds mainly form covalent bonds with other elements [2, 3] and are synthesized through metallurgical processes such as pyrometallurgy and hydrometallurgy. Moreover, the transition metal carbides are utilized in the form of cemented tungsten carbides. These are produced by combining grains of tungsten carbide into a binder matrix such as cobalt (Co) and titanium carbide (TiC), which have many applications because of their hardness and heat resistance [4].

Materials used for cutting tools should have high hardness so as to prevent the effect of heating during the machining process. Tungsten carbide cobalt (WC-Co) is a cost effective material commonly used in industrial machinery to produce cutting tools, abrasives, coatings and corrosion resistance of materials [5, 6]. Most carbides have high melting points which implies that they are stable at high temperatures with high hardness values. Table 1.1 gives a summary of selected properties of different elements.

Table 1. 1: Selected properties of different elements.

Element	Lattice type	Vickers Hardness (MPa)	Shear Modulus (GPa)	Density (g/cm^3)
Tungsten	**bcc**	**3638**	**161**	**19.3**
Iron	**fcc**	**608**	**82**	**7.9**
Cobalt	**hcp**	**1043**	**75**	**8.9**
Titanium	**hcp**	**830**	**44**	**4.5**

Tungsten metal has greatest values of hardness and density compared to those materials in shown in Table 1. These elements can be combine either by chemical reaction or affinity [7].

1.1. Metal carbide alloys

1.1.1. Tungsten carbide cobalt

Wolfram (W) was discovered in the 16th century by miners in Germany. In 1757, Axel Frederik called this metal tungsten due to its density which means "tung" heavy and "sten" stone. In 1906, Henry Moissan received the Nobel Prize in Chemistry for his work on the electric furnace and was instrumental in synthesizing tungsten carbide with a hardness similar to that of diamond [8, 9]. Almost a decade later, Voigtländer and Lohmann [10] conducted a microstructure study on tungsten carbide and found the existence of the two phases: mono-tungsten carbide (WC), and bi-tungsten carbide (W_2C). Tungsten carbide cobalt alloy is an inorganic compound fabricated by sintering WC grains with cobalt as binder cemented together. The hard particle of WC forms the shape of an *extended skeleton* smeared by the Co binder at which the WC-Co alloy has values of density and hardness of about 14.5 g/cm^3 and 1625 HV, respectively [11].

The existence of the WC-Co phase depends on the sintering temperature governed by the "Phase Equilibria in the WC-Co System" [12]. Tungsten amalgamates together with carbon and forms two hexagonally close packed (hcp) carbides, with chemical formulae; WC and W_2C as shown in Figure 1.1 which gives the different phases as function of temperature and carbon composition.

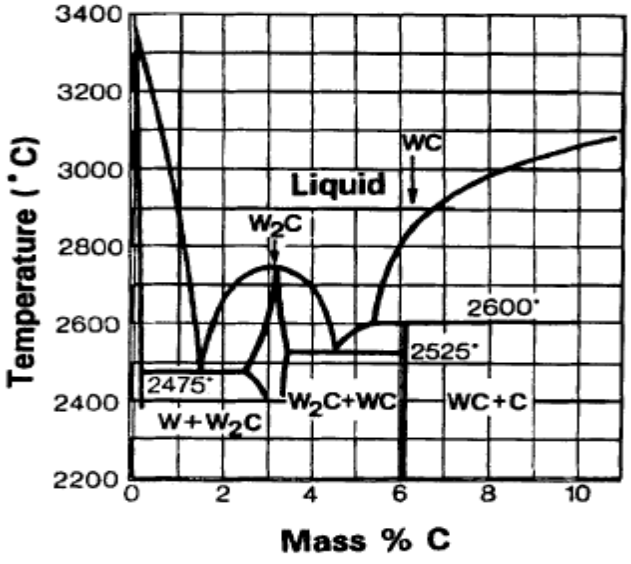

Figure 1.1: Equilibrium phase diagram for the WC binary system [12, 13].

WC contains approximately 6.2% of Carbon and has a micro-hardness of about 2.4×10^3 kg/mm^2, while W_2C contains approximately 3.2% of carbon [11, 14] and has a micro hardness of about 3.0×10^3 kg/mm^2 which is more brittle compared to WC. Among the most frequently used metal carbides, only Mo_2C and WC have a hexagonal closed packed (hcp) crystal structure, whereas NbC, TiC, VC and TaC, are face centred cubic (fcc). The W_2C phase also has other allotropic forms as presented in Figure 1.2.

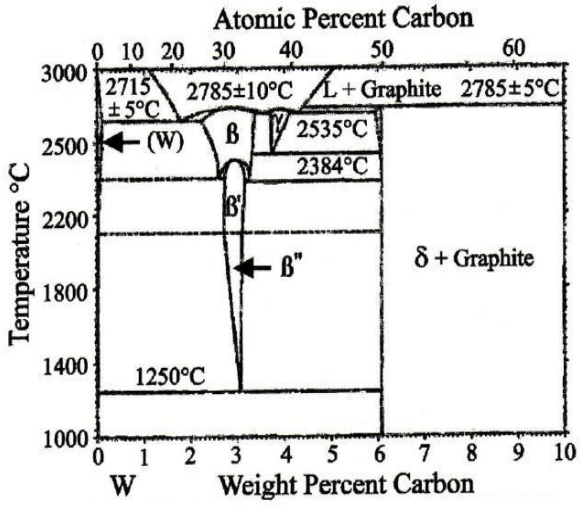

Figure 1.2: An equilibrium phase diagram for the binary W-C system [13].

The wettability and toughness of tungsten carbide with binder metals is better than other carbides (GeC, CaC, SiC) which makes them good candidates to be used as sintered hard metals. Cobalt is generally used as a binder because it has good adhesion properties and exceptional carbide wetting. In addition, Co has a hcp crystal structure at temperature below 428 °C and has a fcc crystal structure above this temperature. At room temperature, a substantial amount of the fcc phase is maintained in sintered WC-Co hard metals and WC-Co coatings [11, 14]. Tungsten carbide without cobalt does not melt under standard atmospheric conditions, however it decomposes into a liquid phase and graphitizes beyond 2780 °C, as illustrated by the phase diagram in Figure 1.2. The compound bi-tungsten carbide

W_2C is metastable at a temperature below 1250 °C and is regularly present in WC-Co, even after relaxed cooling [15].

1.1.2. Titanium carbide

Titanium carbide is a strong refractory ceramic material used for high cutting speed of steel materials and is important for the fabrication of refractory bricks used in lining furnaces, and reactors. Tantalum hafnium carbide (TaHfC) alloy [16, 17] has the highest melting point of 4215 °C compared to all known compounds. For example, TiC has a melting point of about of 3160 °C. Titanium carbide has an elastic modulus about of 400 GPa and a shear modulus of approximately 188 GPa [4]. In powder form [18], it has a black appearance with a fcc crystal structure and is stable at a high temperature of 3066 °C. Therefore, when milled or sintered with other carbides, it is expected that the composite material will have enhanced mechanical and physical properties.

1.2. Literature Review

The high solubility of tungsten carbide in the solid and liquid cobalt binder at high temperatures offer a very good wetting ("adhesion") of WC. Cemented carbides always exhibit substantial toughness due to the partial metallic nature of the composite as compared to Al_2O_3 and SiC which show brittle behaviour. In the tool making industry, materials consisting only of WC and Co alloy have been used for many years due to its exceptional properties such as high melting point, hardness, resistance to heat and high resistance to oxidation. Addition of other carbides, for example TiC have broadened the range of industrial applications of carbides. Thus far, several methods have been successfully applied in producing TiC/Fe composites by combined *in situ* techniques [19, 20]. Other researchers [21] observed that a sintered steel bonded titanium carbide composite was characterized by a substantial improvement in transverse rupture strength and wear resistance.

The sintering of hard materials depends on the size of the particles mixed and the quantity of the samples used. Feng *et al*. [21] demonstrated that in the *in situ* synthesis of the TiC/Fe composite with low volume fraction of TiC by reaction casting that

1 μm TiC particles were homogenously distributed in the iron based matrix. Over the years [22, 23] , a number of research efforts have confirmed that WC has a high melting point of 2870 °C, characterized by extreme hardness with a bulk modulus of 439 GPa, Young's modulus of ~ 550 GPa, and a tensile strength of 345 MPa. It was reported that TiC has an elastic modulus of approximately 400 GPa and a shear modulus of 188 GPa [4]. Other researchers [24, 25] performed Vickers hardness measurements on WC-8TiC-12Co and WC-8TiC-6Co-6Ni and found values of 1395 HV and 1380 HV, respectively. Han *et al.* [26] determined a Vickers hardness value of 1814 HV for WC-10Fe which was in agreement with Bhaumik *et al.* [24]. Table 1.2 gives a summary of selected Vickers hardness values for different binders in the WC matrix.

Table 1.2: Vickers hardness values of different binders in the WC matrix.

Sintered Materials	Binder	Vickers Hardness (HV)	Vickers Hardness (MPa)
WC-10Fe	**Fe**	**1814**	**17790**
WC-10Co	**Co**	**1333**	**13073**
WC-9.6Ni-0.4Co	**Ni-Co**	**1180**	**11572**
WC-8TiC-12Co	**TiC-Co**	**1395**	**13681**
WC-8.7TiN-12Co	**TiN-Co**	**1268**	**12435**
WC-8TiC-6Co-6Ni	**Ti-Co-Ni**	**1380**	**13534**
WC-6TiC-2Mo_2C-6Co-6Ni	**TiC-MoC-Co-Ni**	**1410**	**13828**

Funke *et al.* [27] studied the physical properties of WC-Co and WC-Co-TiC and reported that increasing the Co content resulted in increasing the electrical resistivity because of the binder phases and the addition of TiC reduced the stress of the composite material. X-ray diffraction results [27] have shown that WC-Co-TiC alloys have been subjected to tensile stresses while the WC-Co alloy to compressive stresses.

Over a decade ago, Trindade *et al.* [5] reported a Mössbauer spectroscopy investigation of the role of Fe on sputtered WC films. The Mössbauer spectrum was characterized by one doublet with average hyperfine parameters of isomer shift, δ = 0.26 mm/s and quadrupole splitting, ΔE_Q = 0.53 mm/s. These authors showed that Fe was chemically bonded in WC-sputtered films which contributed to the amorphous nature of the films. The XRD results obtained for the W-C-Co film

showed that 10% Co was present as the amorphous nature and in the W-C-Fe system 8% Fe resembled the amorphous form.

In a recent investigations [28], the relationship of microstructure with wear resistance and hardness in carbide-reinforced ferrous surface composites, TiC milling with other metal alloys (MgF, CrC-MgF) was conducted which resulted in an increase of the hardness of the substrate by a factor of 3 to 4.

In another study, pure iron powder [29] was treated to high-energy ball milling in a hardened steel vial for a period of 30 minutes to 100 hours. The resulting powders were characterized by transmission Mössbauer spectroscopy, XRD and spectrochemical analysis [30]. The results showed that during the ball milling process there was a reduction of the average crystallite size into the nanometer range (from 1 μm to 10 μm) [29, 31] . Increased values for the lattice parameter, magnetic hyperfine spitting and linewidth were also noted.

In the report cited by Zang *et al.* [32], the microstructure of WC-10%Co prepared by ball milling showed that the WC particles was refined to a grain size of 11 nm. The XRD results revealed that the powder sample contained a small portion of the W_2C phase; whilst the Co appeared as fcc (α) and hcp (ε) phases. The grain size reduction during the ball milling process [33] was principally due to the dislocations, annihilation and recombination of small angle grain boundaries separated between individual grains.

Matteazzi *et al.* [34] reported that solid state reaction commences after 12 hours of high energy milling of p-$Fe_{1-x}C_x$ which resulted in the formation of α-Fe phases, hexagonal disordered carbide and cementite (Fe_3C). These authors conducted Mössbauer spectroscopy investigations and found that the room temperature spectrum was characterized by a magnetic structure with a hyperfine field B_{hf} = 20.5±0.2 T and δ = 0.19±0.01 mm/s indicating the presence of Fe_3C; as compared to carburization of iron which is completed after approximately 20 hours. After this period of time, the compound $Fe_{1-x}C_x$ reacted to form orthorhombic Fe_7C_3 carbide.

Over the past twenty years [35], adhesion studies of tungsten carbide cobalt thermally sprayed coating using the indentation test, pull-off test and scanning electron microscopy (SEM) revealed that WC-17Co influenced the adhesion strength. The adhesion strength was found to be proportional to the hardness of the WC-Co coating. Staia *et al.* [35], concluded that the apparent hardness value increased as a function of the grit blasting pressure. Recently, the results obtained by Kin *et al.* [36] was in agreement with Park [37] who showed that Co changed from hcp to fcc crystalline structure after sintering WC-10Co using Spark Plasma sintering (SPS).

Sorescu *et al.* [38] reported on Mössbauer spectroscopy investigations of structural and magnetic properties of $Fe_{50}Co_{50}$ powder using high energy ball milling. The Mössbauer spectrum was characterised by a sextet with a magnetic hyperfine field of about 35 T which revealed the presence of bcc FeCo. These results are in agreement with Akkouche *et al.* [39] who showed that the average B_{hf} = 35 T corresponded to bcc crystalline structure of the solid FeCo solution.

1.3. Aim and objectives of this study

In this work, ^{57}Fe Mössbauer spectroscopy will be employed as the main technique to investigate the structural, electronic and magnetic properties of WC-Co-TiC and WC-Co-TiC-Fe alloys. The aim of the study is to understand how the additional Fe binder affects the properties of the materials under study. Transmission Mössbauer spectroscopy (TMS) and conversion electron Mössbauer spectroscopy (CEMS) measurements were performed on the as-milled powder and the as-sintered WC-Co-TiC-Fe samples, respectively, to monitor the local surroundings of the Fe atoms. In addition, Vickers hardness test, scanning electron microscopy (SEM) and X-ray diffraction (XRD) characterization measurements have been performed. This study is motivated by the fact that low percentage of Fe is unintentionally incorporated in WC and binders from steel balls during the milling process hence to obtain good TMS and CEMS signals, in the materials under study, a reasonably high fraction of 20% Fe has been intentionally incorporated during the milling process. The project has the following objectives:

- To determine the Vickers hardness of the materials,
- To acquire microscopic information on the composition of crystals, morphology, crystalline structure and orientation of the sample by applying scanning electron microscopy (SEM),
- To determine the elemental composition of the material by using Energy Dispersive X-ray Spectroscopy (EDS),
- To establish different phases and the residual strain of the materials using XRD and to ascertain their influence on the hardness of cemented carbides.
- To determine Fe charge states, Fe phases and magnetic effects from hyperfine interaction parameters using TMS and CEMS.

1.4. Dissertation Outline

The introduction, background, literature review of cemented carbides and the aim and objectives of the study are outlined in the current chapter. The theory of the Mössbauer effect, the resultant hyperfine interactions and the principles of X-ray diffraction are discussed in the Chapter 2. Chapter 3 focuses on the experimental details of sample preparation, hardness test, scanning electron microscopy, X-ray diffraction, transmission Mössbauer spectroscopy and conversion electron Mössbauer spectroscopy. The data obtained from these measurements and analysis thereof together with the corresponding results are presented and discussed in Chapter 4. Finally, Chapter 5 gives a summary of the project with conclusions and recommendations. The fitting procedures applied to the data acquired by both the Mössbauer and X-ray spectroscopy methods are described in the appendices.

Chapter 2

Basic Principles of X-ray Diffraction and the Mössbauer Effect

This chapter will introduce the basic principles behind X-ray diffraction and the Mössbauer effect, including a discussion of hyperfine interactions observed, namely electric monopole, electric quadrupole and magnetic dipole interactions.

2.1. X-ray Diffraction

The interaction of radiation and matter has provided several techniques necessary for qualitative and quantitative analysis of materials. X-ray diffraction (XRD) is among the techniques used for this type of analysis, since it can be used to identify the atomic and molecular structure of organic and inorganic crystals.

It is known that solids can be generally categorized as either amorphous or crystalline. In crystalline materials, an ion can occupy a specific location in the regular lattice. In order to make such observations, the crystals must be exposed to finely focused monochromatic beam of X-rays producing a regularly spaced diffraction pattern. The diffraction beam generates a three-dimensional image of the density of the electrons within the crystal. With the aid of Fourier transforms and chemical data, the atomic or molecular structure of the materials, as well as the position of the atoms in the crystal, can be determined.

2.1.1. Bragg planes and Bragg's Law

When a beam of X-rays strikes an ion (electrons) in the crystal, the X-rays are diffracted in all directions and from the scattered X-rays, information about the electron distribution of the material can be determined. Consider two parallel planes of atoms that have the same Miller indices (h, k, l) and are separated by an interplanar distance d, as shown in Figure 2.1 below where θ refers to the angles of incidence or reflection of the beam.

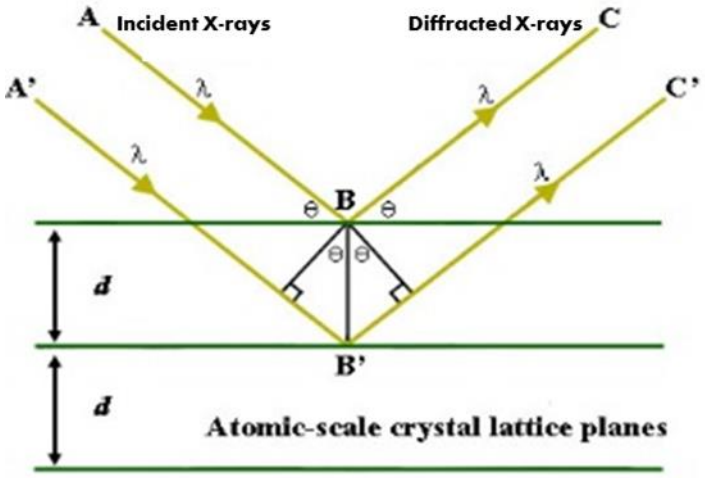

Figure 2.1: Bragg's law derivation from two incident rays on atomic planes [40].

When X-rays strike two adjacent atomic planes at the angle θ, the diffraction condition for constructive interference is given by

$$2d_{\mathrm{hkl}} \sin\theta = n\lambda \qquad (2.1)$$

where d_{hkl} is the interplanar distances, λ is the wavelength of the X-rays, and n is an integer. Note that d_{hkl} depends on the Miller indices and for a simple cubic structure, the lattice constant, a is given by

$$a = \left(\frac{m}{\rho}\right)^{1/3} = d\left(\sqrt{h^2 + k^2 + l^2}\right) \qquad (2.2)$$

where h, k, l are Miller indices of particular planes.

Table 2.1 gives selected wavelengths and energies of typical X-ray source which are always used in the X-ray diffraction technique. The copper X-ray source is the most commonly used source to determine the composition of the materials.

Table 2.1: Different wavelengths and energies of targets at the X-ray source.

Element	Symbol	Kα wavelength (angstrom Å)	Energy (eV)
Silver	Ag	0.559	2.20×10^4
Molybdenum	Mo	0.703	1.75×10^4
Copper	Cu	1.541	1.14×10^4
Cobalt	Co	1.790	0.63×10^4
Iron	Fe	1.937	0.33×10^4
Chromium	Cr	2.294	0.14×10^4

2.1.2. Powder X-ray Diffraction

The powder method is a non-destructive analysis of multiple components primarily used to determine the spacing of atoms in a solid. This method is very accurate, and the results obtained from this approach are easy to interpret. In order for the powder method to return the correct results, monochromatic X-rays must be used and the sample under study must be finely powdered. The data can be obtained using either reflection or transmission geometry as illustrated in Figure 2.2. In the powder method, the particles are randomly oriented in the sample, as a consequence these two methods (transmission and reflection) will yield the same data [41, 42].

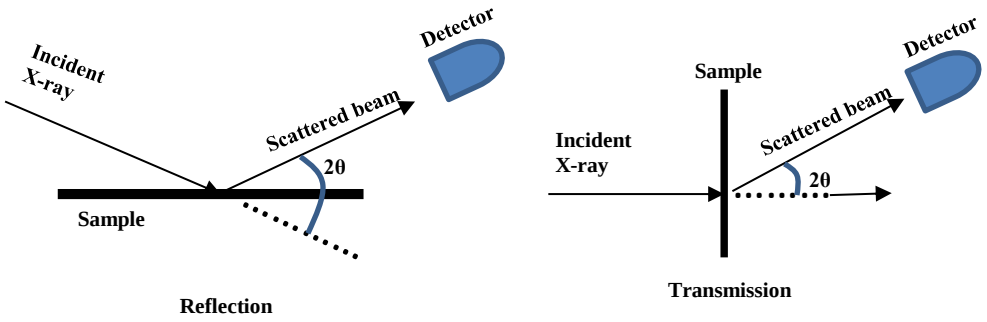

Figure 2.2: Reflection and Transmission geometry of the sample.

For a given inter atomic distance d_{hkl}, there are few values of sin $\theta \leq 1$ that will produce a diffracted beam. Since the sample is in powdery form, the beam will strikes small randomly oriented crystallites so that the diffracted beams corresponding to each distance $d_{hkl,}$ which are necessarily recorded by a rotating

detector around the sample. Therefore, the change in the intensities, the width and position of the peaks are used to identify the structure or the phase of the materials.

2.2. Mössbauer Effect

The Mössbauer effect was discovered in 1958 by Rudolf. L. Mössbauer while working on his doctoral thesis. He observed the recoilless nuclear resonance emission and absorption of gamma rays [43] between nuclei of the same kind (same atomic number Z and neutron number N).

2.2.1. Free nucleus

A free nucleus in the excited state of energy, E_e undergoes a transition to the ground state of energy, E_g by releasing a gamma ray (photon). However, during gamma ray emission, a free nucleus with mass m will experience a recoil with a velocity v in the reverse direction of the gamma ray as shown in Figure 2.3, resulting in loss of energy equal to the kinetic energy or recoil energy, E_R given by

$$E_R = \frac{1}{2} m v^2 . \qquad (2.3)$$

Nucleus of Mass M and energy E_0
(At rest before γ-ray emission)

Figure 2.3: Momentum $\vec{P}_n$ and E_R energy lost by a free nucleus upon γ-ray emission.

As shown in Figure 2.3 equation 2.3 can be written in the form

$$E_R = \frac{P_n^2}{2m} = \frac{E_0^2}{2mc^2} . \qquad (2.4)$$

P_n and P_γ represent the momenta of the nucleus and γ-ray respectively, E_0 is transition energy between excited and ground states, m is mass, c is the speed of the light in vacuum. As a result, resonant emission and absorption processes cannot be observed because the gamma ray energy (E_γ) is lower than the transition energy because of the loss in energy due to recoil. Thus, the energy carried by the emitted gamma ray is given by

$$E_{\gamma} = E_0 - E_{\mathrm{R}} . \qquad (2.5)$$

This is illustrated by Figure 2.4.

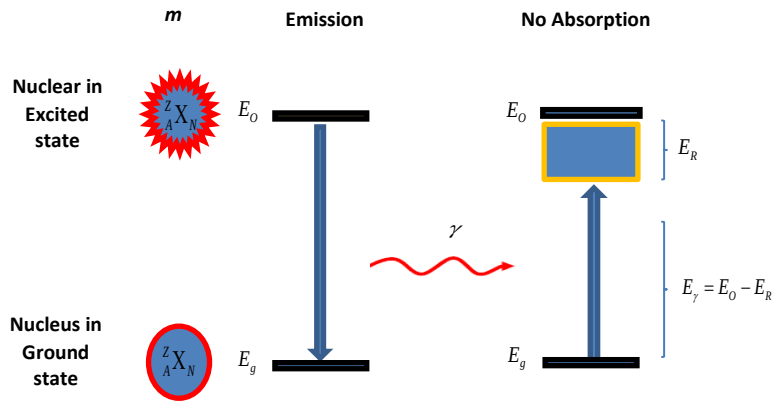

Figure 2.4: Lack of resonant γ-ray absorption due to energy recoil lost by the nucleus.

2.2.2. Mössbauer active atom is rigidly bound to the lattice

When the nucleus is rigidly bound in the crystal lattice of mass *M*, the recoil energy is taken up in lattice vibrations. Because the mass of the crystal is very large compared to the mass of the nucleus ($M >> m$), it follows that, E_{R} becomes negligible. Thus, the energy carried by the gamma ray is approximately equal to the transition energy between the excited state and ground state suggesting the possibility of observing resonant emission and absorption between two nuclei as depicted in Figure 2.5 (a) and (b).

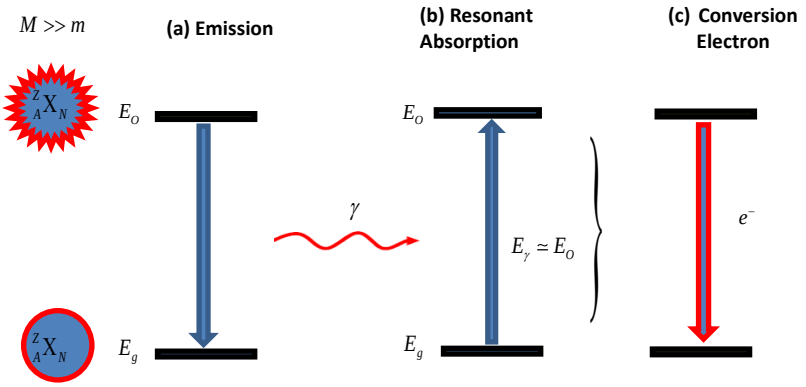

Figure 2.5: Resonant emission and absorption of γ-ray in the nucleus bound in the lattice and conversion electron.

After resonant absorption, the excited nucleus can de-excite to the ground state by re-emission of a gamma ray or by emission of conversion electrons as show in Figure 2.5 (c).

2.2.3 Natural Linewidth

The natural line width (Γ) according to Heisenberg uncertainty principle is given in terms of energy uncertainty with mean lifetime (τ_N) by

$$\Gamma = \frac{\hbar}{\tau_N} \tag{2.6}$$

where $\hbar$ is equal to h (Planck's constant) divided by 2π and mean lifetime is the product of the half-life ($\tau_{1/2}$) and ln2. The ^{57}Fe nucleus is utilized as an isotope with the 14.4 keV Mössbauer state and a mean lifetime of 141 ns. This offers an energy resolution value of approximately $\Gamma = 5\times10^{-9}$ eV resulting in an energy ratio about $E_\gamma/\Gamma = 3.1\times10^{12}$. Mössbauer spectroscopy has the highest energy resolution of 5×10^{-9} eV compared to any other spectroscopic method [44]. The distribution of energies about E_0 is given by the Breit-Wigner form by

$$I(E) = \frac{(\Gamma/2)^2}{(E-E_0)^2 + (\Gamma/2)^2} \tag{2.7}$$

where, Γ gives the Full Width at Half Maximum (FWHM) of the resonance spectral line. This is graphically illustrated in Figure 2.6.

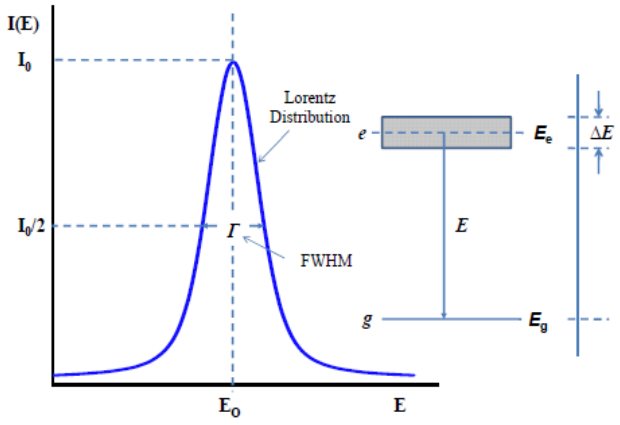

Figure 2.6: Intensity *I* (*E*) plotted against transition energy *E* [45].

The resonance absorption cross section is given by

$$\sigma(E) = \frac{\sigma_0 \Gamma^2}{4(E - E_0) + \Gamma^2} \tag{2.8}$$

where

$$\sigma_0 = \frac{\lambda^2}{2\pi} \frac{2I_e + 1}{2I_g + 1} \frac{1}{\alpha + 1}. \tag{2.9}$$

The term σ_0 represents the maximum absorption cross section, λ is the wavelength of the gamma ray; I_g and I_e are the nucleus spin quantum numbers of respective states and α is the internal conversion coefficient.

2.2.4. Recoil free fraction

When the nucleus of gamma ray emitting (or absorbing) atom is embedded in a crystal lattice, the recoil energy is transferred to lattice vibrations to the atom and then dissipate as a heat, taking into account the Einstein's model of solids, there exist a possibility of transition without lattice vibrations (zero-phonon transitions) [46, 47, 48]. This probability is commonly referred to as the recoil-free fraction and can be mathematically as expressed in the form

$$f = 1 - k^2 \langle x^2 \rangle \tag{2.10}$$

where $\langle x^2 \rangle$ represents the mean square displacement of the nucleus in the x direction of the incoming gamma ray and k is the propagation vector. The more general expression for f is

$$f = \exp\left(-k^2 \langle x^2 \rangle\right). \tag{2.11}$$

In addition, f can be further calculated in the Debye's model to give

$$f = \exp\left[-\frac{E_R}{k_B \Theta_D}\left(\frac{3}{2} + \frac{\pi^2}{\Theta_D^2} T^2\right)\right] \qquad \text{for } T \ll \Theta_D \tag{2.12}$$

$$f = \exp\left[-\frac{6E_R T}{k_B \Theta_D^2}\right] \qquad \text{for } T \geq \Theta_D \tag{2.13}$$

where, Θ_D is the Debye temperature and k_B is the Boltzmann's constant.

From equations 2.12 and 2.13,

- f is dependent on the temperature,
- f increases inversely proportional to E_R and
- f increases with a decrease in the Debye temperature.

The latter expression gives information on the strength of bonds between the Mössbauer atom and the lattice [46].

2.2.5. Hyperfine interaction parameters

Mössbauer spectroscopy has a highest energy resolution of 5×10^{-9} eV as compared to other spectroscopic method, and can distinguish the slightest changes in the nuclear environment of an atom involved [48, 49, 50]. Generally there are three types of nuclear interactions, namely, electric monopole, electric quadrupole and magnetic dipole interaction.

2.2.5.1. Electric monopole interaction: Isomer shift

The isomer shift describes the shift in nuclear energy levels between the source and absorber, owing to the electric monopole interaction between the *s*-electrons and the nucleus. The resulting changes in the nuclear energy levels as illustrated in Figure 2.7 (a), results in a shift of the resonance peak is shown in Figure 2.7 (b).

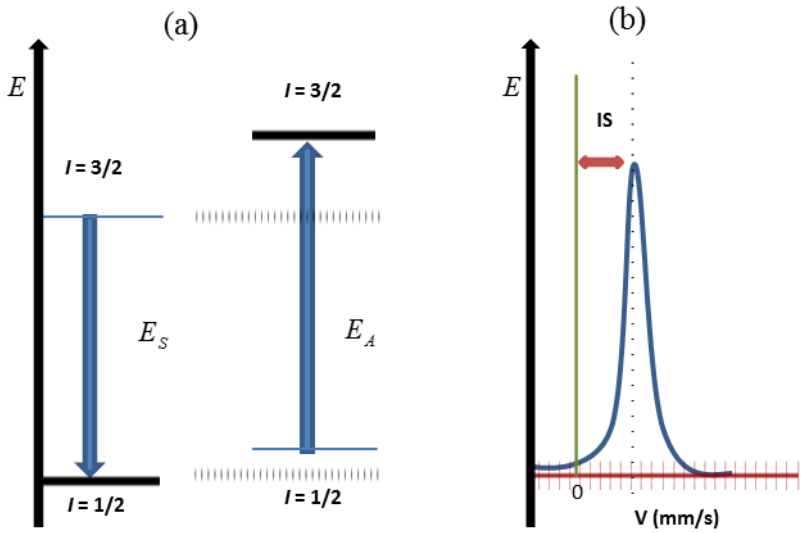

Figure 2.7: **(a) The changes in the nuclear energy levels in the source and absorber and (b) resulting shift in the Mössbauer spectrum.**

When the source and absorber moves relative to each other, the observed difference of the electrostatic shifts of the source and absorber [51, 52] is given by

$$\delta = \delta_{\mathrm{A}} - \delta_{\mathrm{S}} = \frac{2}{3}\pi Ze^2\left(\left|\psi_{(0)}\right|_{\mathrm{A}}^2 - \left|\psi_{(0)}\right|_{\mathrm{S}}^2\right)\left[\left\langle r^2\right\rangle_{\mathrm{e}} - \left\langle r^2\right\rangle_{\mathrm{g}}\right] \qquad (2.14)$$

where δ_{A} and δ_{S} are the electrostatic shifts of the absorber and source, respectively. $\left|\psi_{(0)}\right|_{\mathrm{A}}^2$ and $\left|\psi_{(0)}\right|_{\mathrm{S}}^2$ are the *s*-electron densities at the nuclei of absorber and source, respectively, *r* is the nuclear radius and Ze^2 is the nuclear charge.

This shift in the position of resonance peak from zero velocity is known as the *isomer shift* (δ) (see Figure 2.7 (b). In the case of a heavier element, the wave function Ψ is extensively modified by relativistic effects to give

$$\delta = \frac{4}{5}\pi Ze^2 S'(Z) R^2 \frac{\delta R}{R}\left(\left|\psi(0)\right|_{\mathrm{A}}^2 - \left|\psi(0)\right|_{\mathrm{S}}^2\right). \qquad (2.15)$$

The term *S'*(*Z*) is the relativistic factor and *δR/R*, which stands for relative modification of the nuclear radius in going from the excited state to the ground state[52]. The isomer shift offers valuable information about the charge state of a Mössbauer atom as well as the electronegativity, coordination number, valence and bond properties [46, 51]. The electron density can be related to oxidation state and chemical surroundings of the atom e.g. ferric ionic (Fe^{3+} oxidized) has a lower isomer shift than the ferrous ion (Fe^{2+}) due to the electron density of the ferric ion at the nuclei which is higher because of a lower shielding effect by *d* electrons. The δ-values become more positive by reducing the formal oxidation state [50]. Figure 2.8 gives a selection of isomer shift values perceived in ^{57}Fe compounds for different cations and spin states of ^{57}Fe.

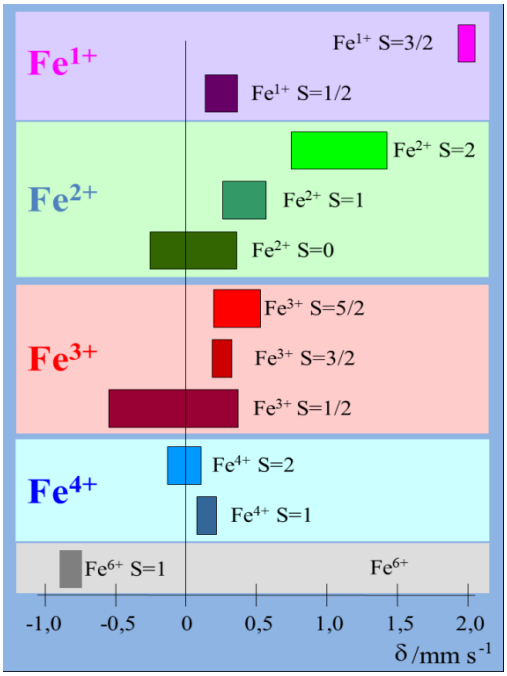

Figure 2.8: **Isomer shift values and oxidation states observed for ^{57}Fe compounds measured at room temperature [53].**

2.2.5.2. Electric quadrupole interaction: Quadrupole splitting

Quadrupole splitting reveals the interaction between nuclear quadrupole moment and the electric field gradient (EFG) created by the distribution of electronic charge around the nucleus. Therefore, in the case of ^{57}Fe, the ground state with $I = 1/2$ is unsplit because there is no recognisable spectroscopic quadrupole moment [46, 49], as nucleus is spherical while for $I > 1/2$, there is a quadrupole moment as nucleus is non-spherical. The electric field gradient interacts with the non-spherical charge distribution to lift the degeneracy thus the $I = 3/2$ state is divided into two sub-states with quantum numbers, $m_I = \pm 1/2$ and $m_I = \pm 3/2$. This allows for two transition which result in two resonance lines as shown in Figure 2.9 giving a doublet in the spectrum governed by the selection rule ($\Delta m = 0, \pm 1$).

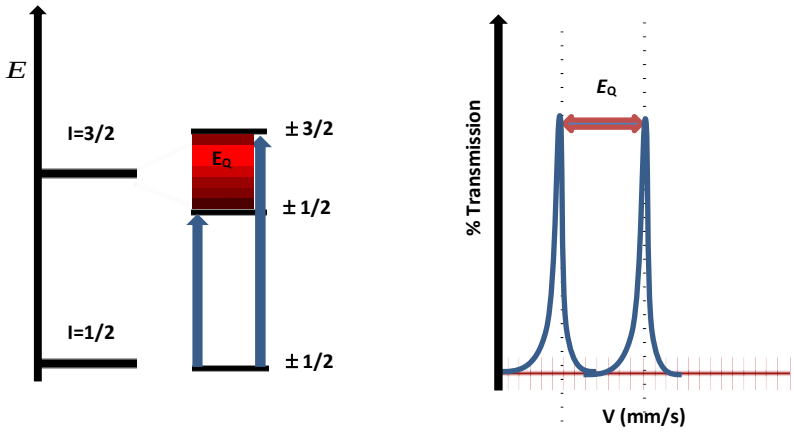

Figure 2. 9: Quadrupole splitting nuclear level and the resultant Mössbauer spectrum.

The quadrupole splitting is observed as the 'distance' between these two peaks, reflecting the change in nuclear energy between the sub-states [47] given by

$$\Delta E_{\mathrm{Q}} = \frac{eQV_{zz}}{2} \tag{2.16}$$

where V_{zz} denote the principal axis of the EFG. From perturbation theory, the eigenvalue E_{Q} can be given by the formula

$$E_{\mathrm{Q}} = \frac{eQV_{zz}}{4I(2I-1)}\left[3m_1^2 - I(I+1)\right]\left(1+\frac{\eta^2}{3}\right)^{1/2} \tag{2.17}$$

where e is the elementary charge, η is the asymmetry parameter calculated from the second derivatives of the electric potential V (see equation 2.19).

The information about the electronic and molecular structure can thus be obtained from the quadrupole interaction originating from changes in the electric field gradient [54, 55].

The interpretation of quadrupole splitting consequently require understanding about the source of EFG and the manner it is changed by physical and chemical influences.

The following conditions are necessary for the electric quadrupole interaction to occur:

- There must be an observable nuclear quadrupole moment and
- Non-zero electric field gradient at the nucleus.

The Laplace equation requires that the electric field gradient be a traceless tensor,

$$V_{zz} + V_{xx} + V_{yy} = 0 . \tag{2.18}$$

The EFG has two independent parameters [56]; V_{ZZ} denoted as eq (e = proton charge) and the asymmetry parameter η given by

$$\eta = \frac{V_{xx} - V_{yy}}{V_{zz}} \quad \text{where} \quad V_{xx} = \frac{\partial^2 V}{\partial x^2} . \tag{2.19}$$

By considering the principal axes such that the ordering $|V_{zz}| \geq |V_{xx}| \geq |V_{yy}|$. Each of these reflect two sources which can contribute to the total electric field gradient:

- Lattice contribution (ions which surround the Mössbauer atom in non-asymmetric) given by

$$V_{ZZ} = (1-\gamma_\infty)(V_{zz})_{lat} + (1-R)(V_{zz})_{Val} \tag{2.20}$$

- Valence electron contribution (anisotropic electron distribution in the valence shell of the Mössbauer atom) given by

$$\eta = \frac{1}{V_{zz}}\left[(1-\gamma_\infty)(V_{zz})_{Lat}\,\eta_{Lat} + (1-R)(V_{zz})_{Val}\,\eta_{Val}\right] \tag{2.21}$$

where the term γ_∞ is the Sternheimer anti-shielding factor which corresponds to a value of about -9.43 for trivalent Fe^{3+}, and R is a known dimensionless constant given in the range 0.2-0.3 [57, 58].

2.2.5.3. Magnetic hyperfine interaction: hyperfine magnetic splitting

The magnetic hyperfine interaction reflects the interaction between the nucleus and total effective magnetic field [49] present at each nucleus site. For the nuclear spin quantum number $I > 0$, a nucleus of spin I, the magnetic field lifts the degeneracy resulting into $2I+1$ sub-levels. For example, a nucleus with spin state $I = 3/2$ in case of ^{57}Fe is divided into four non-degenerate sub-states with m_I values 3/2, 1/2, -1/2

and -3/2 and similarly for I = 1/2 one obtains two sub-levels 1/2 and -1/2. The selection rules for the magnetic dipole transition (Δm = 0, ±1) allow for gamma transitions between the sublevels six possible transitions resulting in six absorption lines in the Mössbauer spectrum. Figure 2.10 shows the six possible transitions for 3/2 and 1/2 resulting in six lines (nuclear Zeeman Effect) which are collectively referred to as a sextet.

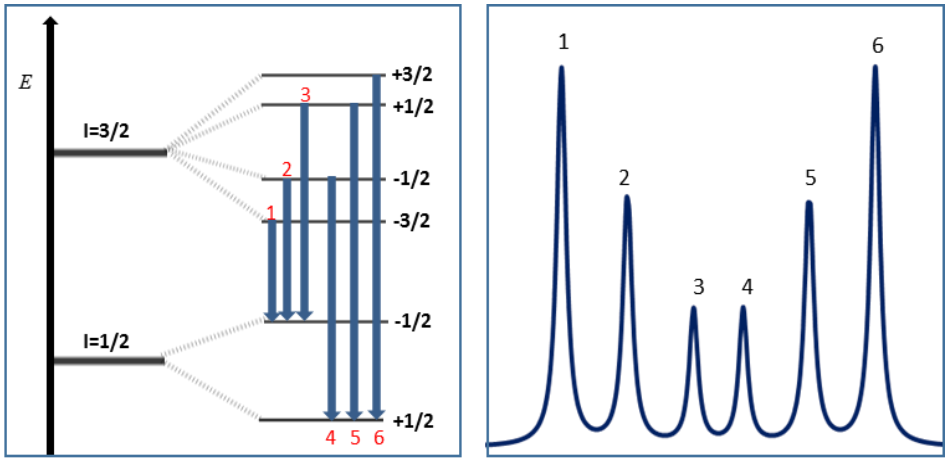

Figure 2.10: **Magnetic splitting of the two nuclear levels I = 3/2 and I = 1/2 and the corresponding spectrum.**

The magnetic hyperfine interaction can be defined by the Hamiltonian given by the expression

$$H_m = -\mu B = -g_I \mu_N I B_z \qquad (2.22)$$

where μ represents the magnetic moment of the nucleus, μ_N is the nucleus magneton and g_I is the gyromagnetic factor of the nucleus having a nuclear spin I.

Magnetic dipole splitting provides information concerning spin interaction processes. Information can be inferred from the magnetic relaxation moment, electron configuration, spin value, magnetic transition temperature and spin flop processes [51].

Chapter 3

Experimental Details

This chapter describes the synthesis of the samples selected for this study and the various techniques applied in experimental work: Vickers hardness, microstructure, X-ray diffraction and Mössbauer spectroscopy in order to characterize the materials under study. In addition, a description of all the equipment used and how the respective measurements were carried out will be presented. Finally, much attention is given to the experimental details of Mössbauer spectroscopy which is the main technique applied in this study.

3.1. Synthesis procedures

3.1.1. Preparation of samples

Two samples were prepared: (a) WC-10Co-6TiC powder was obtained by mixing 84.58 g of WC, 10.28 g of Co and 6.33 g of TiC powders and (b) WC-10Co-6TiC-20Fe powder was obtained by adding Fe20-wt% to WC-10Co-6TiC. In addition 2.04 g of polyethylene glycol (PEG), 32.50 ml of ethanol and 0.24 g of dispersant were used to facilitate the reaction during mixing. Table 3.1 gives the particle size (in micrometres) of the starting materials which is the key parameter used as an indicator for the good mixture of the powders.

Table 3.1: Different particle sizes of the starting materials.

Material	WC	Co	TiC	Fe
Size (μm)	4.5±0.2	0.9±0.05	1.6±0.02	5.0±0.2

3.1.2. Milling procedure

Powder samples of WC-10Co-6TiC-20Fe were obtained by adding Fe20-wt% and WC-10Co-6TiC in exact proportions to ensure that chemical reactions occur during the process. The samples were ball milled for 15 hours at a rotational speed of 140 rpm using the tungsten carbide ball to powder weight ratio of 5:1. An organic binder (PEG) was used to facilitate the mobility of the particles and was eliminated during the heat treatment. After milling, the samples were dried by using a rotator

evaporator at a speed of 80 rpm and at a temperature of approximately 60 °C for a period of 45 min using a powder to ethanol weight ratio of 3:1.

3.1.3. Sintering procedure

In liquid phase sintering, the powder samples were pressed into a green compact and then sintered using an ULTAR-TEMP Sinter furnace – HIP series model (Pilot Tools Facility). The green compact was placed in a heating chamber and heated under a pressure of approximately 0.04 MPa at a starting heating rate of approximately of 2.4 °C per minute to 270 °C. To tolerate a good flow of hydrogen gas inside the heating chamber for dewaxing, the temperature was kept constant for approximately 1 hour 5 mins and the vacuum pump switched off. This process was to facilitate the entire elimination of polyethylene glycol compound in the samples.

The dewaxing process comprised of four stages utilizing a chain of heating rates and dwell times with a temperature range from 270 °C to 450 °C which facilitates the entire elimination of the polyethylene glycol compound in the samples. After the dewaxing process, the hydrogen gas was removed by keeping the temperature at 450 °C for a supplementary time of 20 minutes during which the vacuum pump was turned on to ensure that the system is free of any residual chemicals. The heating rate of about 4.2 °C per minute was then applied in the temperature range of 450 °C to 1000 °C. Each temperature was maintained constant for 5 mins with the vacuum pump switch off to ensure a good flow of hydrogen and methane for carbon correction. The carbon control was operated for 1.5 hours while the vacuum pump was turned on to ensure that hydrogen and methane were eliminated [59]. Carbon correction was required to verify whether the carbon was lost, replaced or persisted in the system during dewaxing.

The heating rate of 3.3 °C per minute was performed from 1000 °C to 1200 °C; at the threshold temperature of 1200 °C cobalt loss protection (CLP) was used in an argon gas environment of 0.37 MPa. In this case, CLP was operated at heating rate of 3.5 °C per minute and a temperature up to 1430 °C. The temperature was kept constant for a period of about 1.25 hours and for 20 minutes during the end of the

cycle, hot isostatic pressing (HIP) was made at the pressure of about 4.4 MPa to ensure that porosity was eliminated [59]. Finally, the furnace was cooled down using water at a rate of about 3.5 °C per minute. The Fe20-wt% with WC-10Co-6TiC mixture was sintered offering the possibility of formation of a number of possible complexes such as TiFe, FeC, FeCo, FeWC, FeCoW, Fe-WC-Co-TiC and FeTiC.

3.1.4. Polishing procedure

The samples were cut into cylindrical shapes with the thickness and diameters of 0.92 mm and 40 mm, respectively. Then, the samples were mounted using an ATA opal 410 hot mounting press machine in preparation for use in the polishing machine. The polishing was conducted by applying a force of 5 N and speed of 60 rpm for 5 minutes using a steel diamond plate and micro plate 1 to 6 μm at a speed of 120-150 rpm for 3 minutes to make the samples smooth like a mirror. Figure 3.1 shows a photograph of the Strues Polisher machine used to remove all damages on the surface of the samples to ensure a surface acquires a mirror like finish. The polished samples were used for hardness, SEM/EDS and X-ray diffraction measurement whilst the unpolished samples were used for TMS and CEMS measurement.

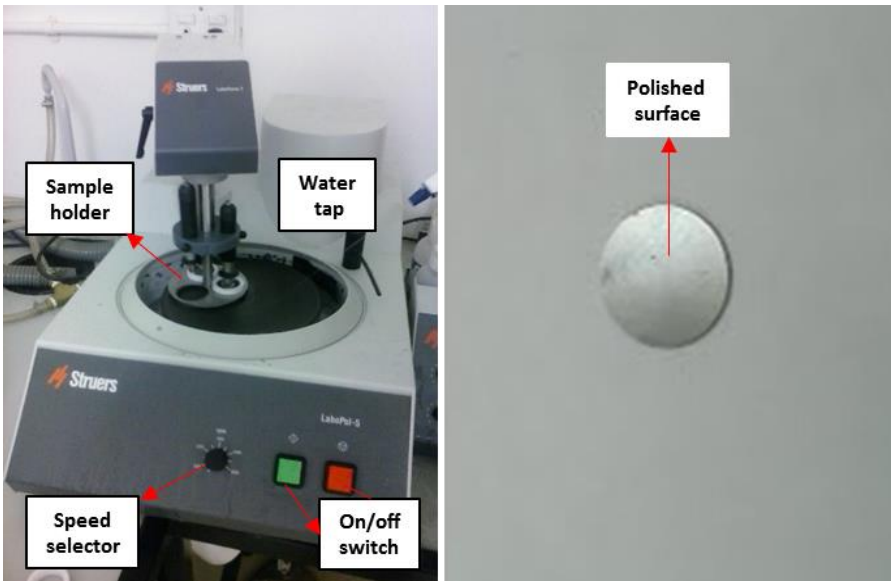

Figure 3.1: Strues Polisher machine and polished sample.

3.2. Characterisation techniques

3.2.1. Vickers hardness

The Vickers hardness machine for micro and small force range [60], operates as follows: the application of a determined force is controlled with the use of a computer. A force is exerted on the surface of a material. This is followed by the measurement of the diagonal from the resulting impression after removal of the force on the material under test. Figure 3.2 illustrates the Vickers hardness indention while Figure 3.3 shows the Future-tech FM 800 testing machine.

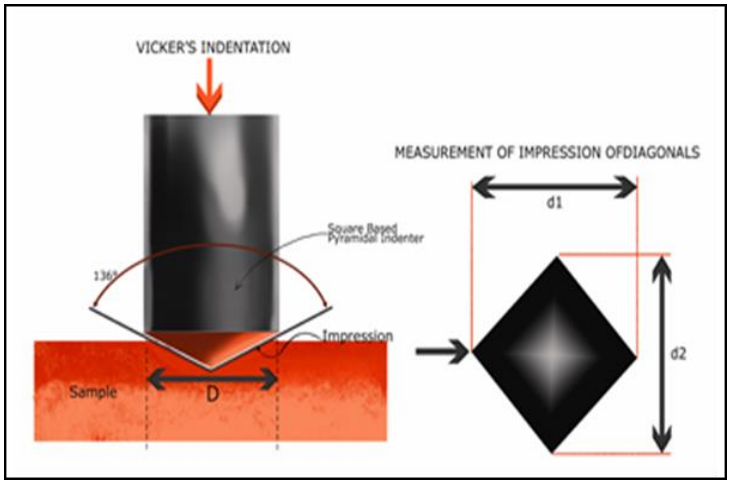

Figure 3.2: Basis of the Vickers hardness indention [61].

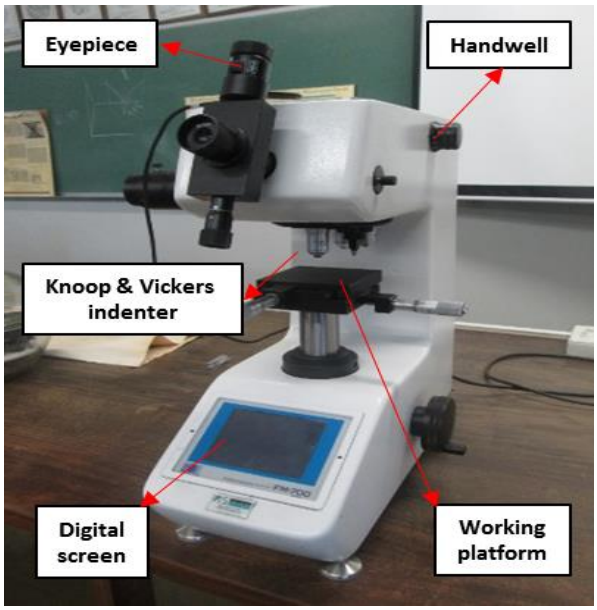

Figure 3.3: Future-tech FM800 micro Vickers Hardness testing machine.

The polished sample was pressed with a micrometer diamond indenter for 15 seconds using a load of 500 g [62]. The Vickers hardness values were obtained, measurements based on the formula

$$HV \simeq \frac{1.8545 \times 10^3 P}{d^2} \tag{3.1}$$

where P refers to force in gramme-force (gf) and d is the diagonal impression measurement expressed in mm.

The mean diagonal impression, D (in mm) is given by

$$D = \frac{d_1 + d_2}{2}. \tag{3.2}$$

3.2.2. Scanning Electron Microscopy with Energy dispersive X-ray

Field emission scanning electron microscopy (FESEM) data were obtained using a Carl Zeiss Sigma machine dual with energy dispersive X-ray spectroscopy with an Oxford X-act detector. The microstructure and morphology of the samples were measured using a computer operated with Zeiss Smart SEM version 5.06 interface software and INCA suite version software to ensure qualitative and quantitative analysis of the samples. Figure 3.4 shows the Carl Zeiss Sigma FESEM instrumentation whilst Figure 3.5 shows a schematic diagram set-up of scanning electron microscopy with energy dispersive X-ray spectroscopy in detail.

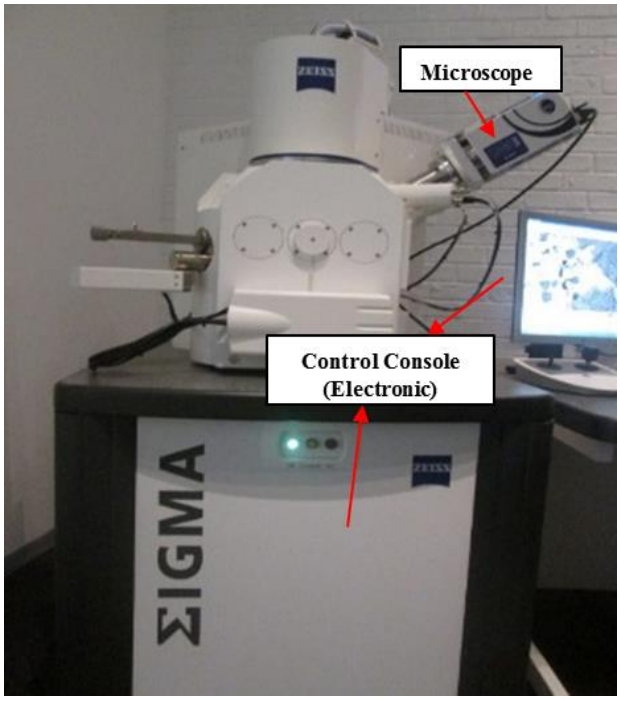

Figure 3.4: Carl Zeiss Sigma field emission scanning electron microscopy (FESEM).

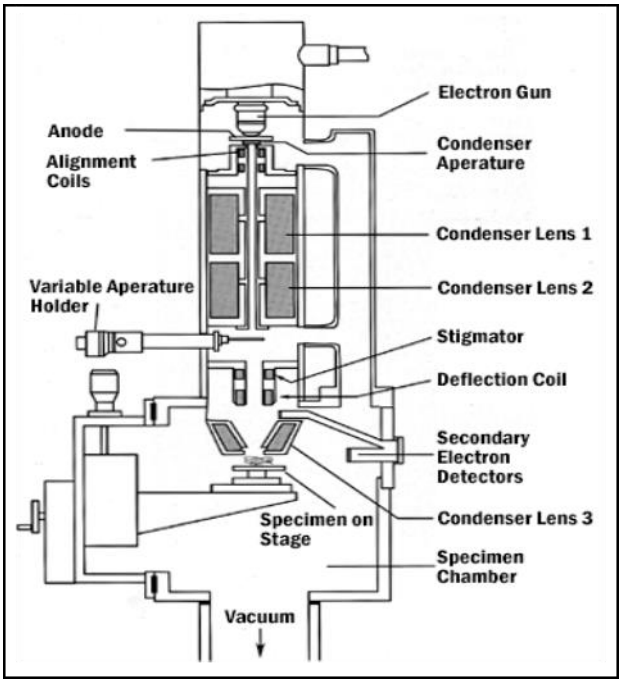

Figure 3.5: Schematic diagram of a scanning electron microscope [63].

3.2.3. X-ray Diffraction and strain analysis

The Bruker D2 Phaser X-ray diffractometer was utilized to obtain the diffraction patterns in order to determine the chemical composition of the samples at room temperature. The X-ray diffraction measurements were performed using cobalt radiation operated at a voltage of 30 kV and a current of 10 mA with a LynxEye detector. A 0.6 mm slit was in operation with a 3 mm air scatter slit. The patterns were collected at a step size of 0.026° from 20°-100° value of 2θ for 10 minutes.

The diffraction patterns obtained from the spectrometer were analysed using the Diffrac-Plus EVA Software which works either in two or three dimensions. The qualitative analysis was performed using this software, which identifies spectral components using a database. This analysis provides important information about the particle size and phase matching. Figure 3.6 shows an illustration of the X-ray diffraction spectrometer.

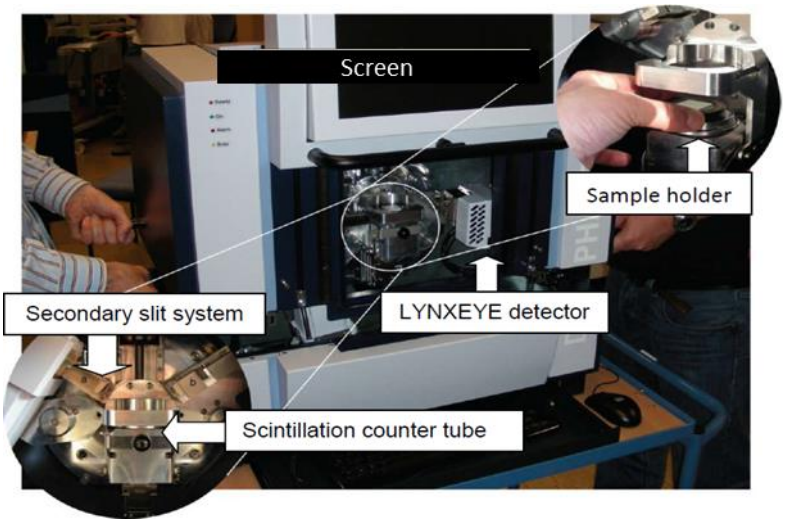

Figure 3.6: Illustration of the X-ray Diffraction machine [40].

Many techniques can be used to determine the stress and strain of sintered materials such as X-ray diffraction, hole drilling technique, layer removal and analytical method [64, 65, 66]. In the present work, X-ray diffraction was used to obtain information about the samples and the residual strain was determined in accordance with the Topas description defined in the Topas manual (v4-2) and from the research work undertaken by Balzar *et al*. [67].

3.2.4. Mössbauer spectroscopy

^{57}Fe Mössbauer spectroscopy was the main characterization technique used in this study. It serves as an excellent method for the study of impurities, and can be utilized to determine Fe site location, Fe phases, Fe charge state and Fe site population. The Mössbauer hyperfine parameters describes the interactions between surrounding electrons and nuclei and can give detailed information about the isomer shift, quadrupole splitting and magnetic splitting. In the case of the present work, transmission Mössbauer spectroscopy (TMS) and conversion electron Mössbauer spectroscopy (CEMS) were used for the characterization of the powder and sintered samples, respectively.

3.2.4.1. Transmission Mössbauer spectroscopy

The parent isotope ^{57}Co decays by electron capture to the 136.3 keV energy level of excited ^{57}Fe* with quantum number of $I = 5/2$ which then decays after 10 ns and populates, with 85% probability the 14.4 keV level by emitting a 122 keV photon. Thereafter, with a possibility of 15% the 136 keV energy level decays to the ground state of ^{57}Fe. For the 14.4 keV transition [55] as shown in Figure 3.7.

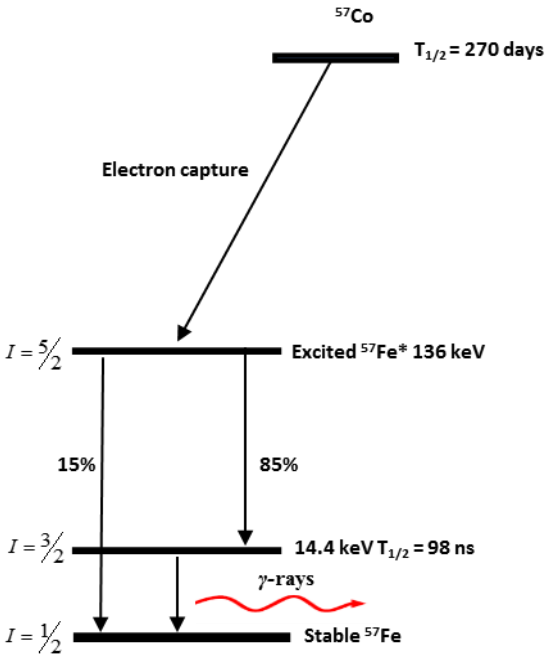

Figure 3.7: Nuclear decay scheme of ^{57}Co.

The source is mounted on a vibrator, which moves back and forth at a certain velocity, which results in a Doppler shift of the recoilless γ-rays to be achieved. The source under the control of a velocity transducer can move back and forth at constant acceleration, either sinusoidally or in a symmetric saw tooth. Therefore, the Doppler energy as well as the energy of gamma quanta can be Doppler shifted in a *controllable* manner [47, 51].

The Doppler shifted γ-rays can pass from the source through the absorber (powder sample) and some can be resonantly absorbed by an identical Mössbauer probe isotope in the source, thereafter the absorber emits the γ-rays from the source after penetration. Figure 3.8 illustrates the arrangement of Mössbauer equipment at the Wits University Mössbauer Laboratory.

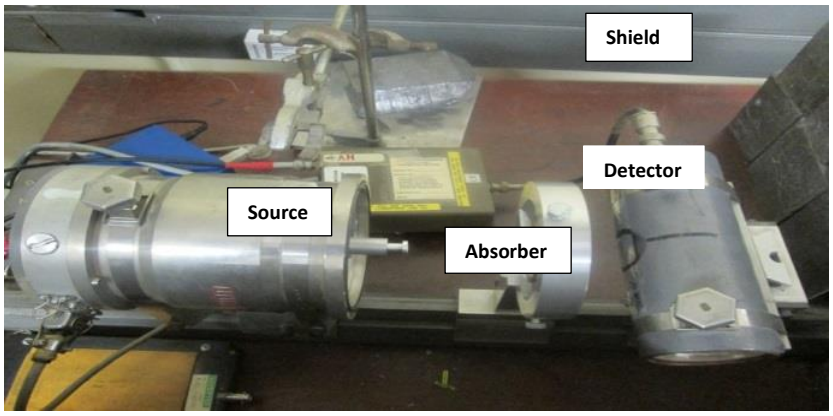

Figure 3.8: Typical geometry of transmission Mössbauer spectroscopy.

The gas proportional counter filled with $KrCO_2$ (PA-700) at the pressure about of 2 atm was used as a detector to record the γ-rays emitted from the absorber. The electronic instrumentation for both transmission Mössbauer and conversion electron Mössbauer spectroscopy are almost identical and will be discussed in detail in section 3.2.4.3. Figure 3.9 shows the arrangement of electronic modules used in transmission Mössbauer spectroscopy.

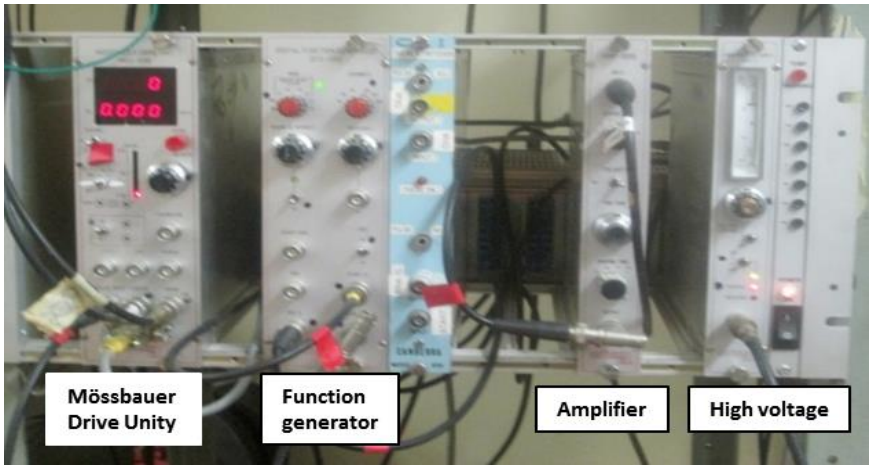

Figure 3.9: Experimental arrangement of Mössbauer spectroscopy.

3.2.4.2. Conversion electron Mössbauer spectroscopy

Conversion electron Mössbauer spectroscopy is a suitable technique for surface characterization of solid materials. In this technique, γ-rays released from the source experience recoilless absorption in the "CEMS-Sample", the excited Mössbauer nuclei and then de-excite according to an intrinsic life-time to generate the conversion electrons which are then detected. A parallel-plate avalanche detector (PPAD) developed at WITS, has been utilized as the detector [68]. As shown in Figure 3.10 below, γ-rays from the source strike a sample incorporated in the PPAD. Unpolished samples with a thickness of about 0.92 mm was used in CEMS measurements.

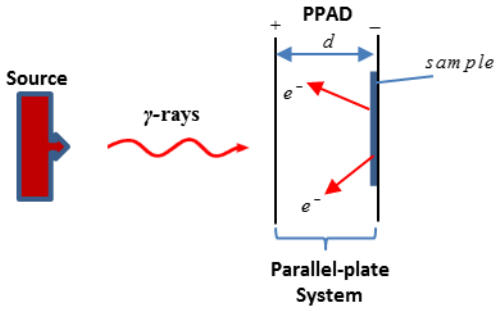

Figure 3.10: Schematic diagram of PPAD with a source of γ-rays.

CEMS measurements were conducted at room temperature. The sample to be probed was placed in the PPAD on one of the plates which was negatively charged

as shown in Figure 3.11. The bias voltage was set by increasing the high voltage until the count appears in the screen.

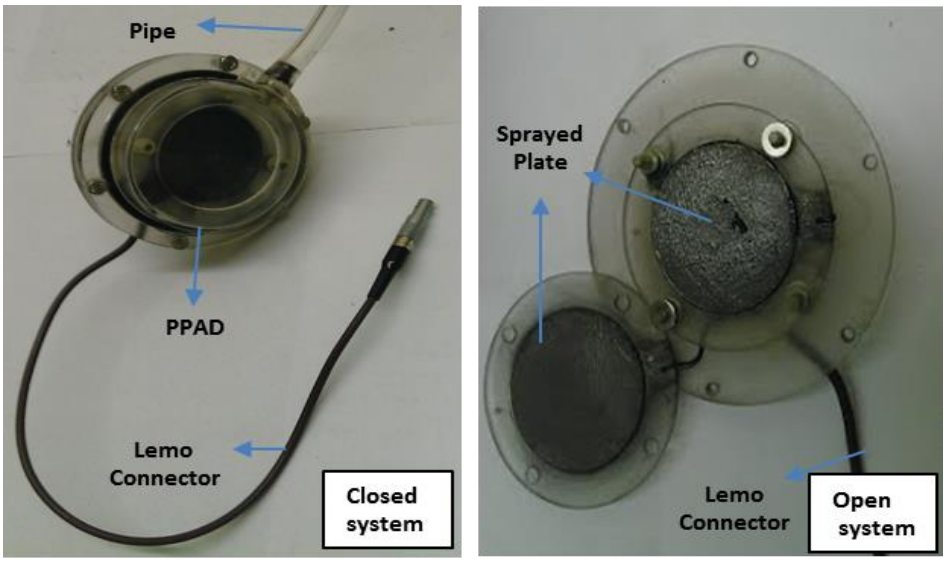

Figure 3.11: Schematic diagram of the closed and opened PPAD system.

The graphite layers were made by spraying both sides of the plates for conductivity so that it is making possible the mobility of the electrons. Moreover, the pipe must be connected to the tank while the Lemo connector was connected to the pre-amplifier. The procedures of the operation of the pumping acetone vapour is gives in section 3.2.4.4.

3.2.4.3. Principles of Conversion electron Mössbauer spectroscopy

The parent isotope ^{57}Co decays by electron capture and firstly populates the 136.3 keV energy level of ^{57}Fe, and then 91% probability to the 14.4 keV energy level by emitting a 122 keV photon. Thereafter, with a probability of 9% the 136 keV energy level decays to the ground state of ^{57}Fe. Figure 3.12 shows that for the 14.4 keV transition, ~11% result in the emission of γ-rays, while the remaining 89% result in the transfer of the transition energy to an electron (conversion electron). It utilizes the *K*, *L* and *M* electron to investigate the top 200-300 nm of a surface of the sample [50, 68]. Approximately, 7.3 keV, 13.6 keV and 14.3 keV energy result from the *K*, *L* and *M* shells, respectively.

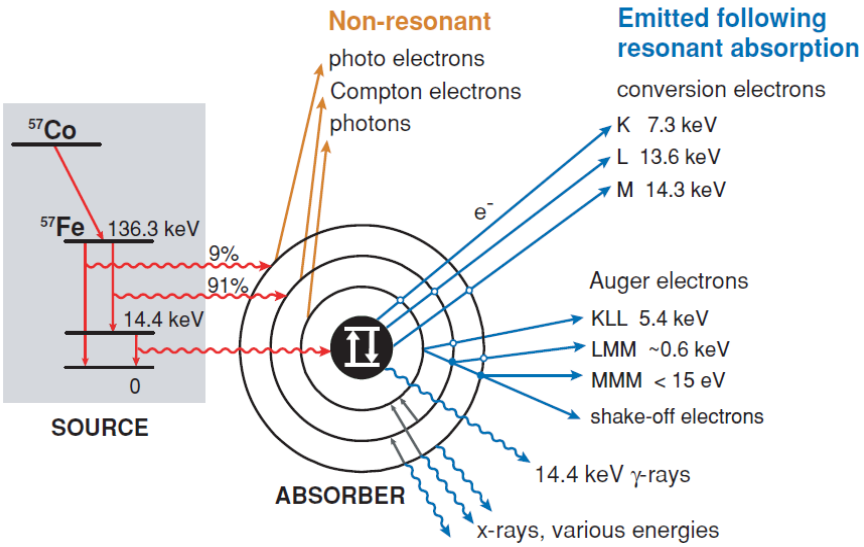

Figure 3.12: The nuclear decay scheme for ^{57}Co and various backscattering processes for ^{57}Fe that can follow resonance absorption of an incident gamma photon, modified from De Grave *et al.* (2005) [69]. The transition probabilities recorded in this Figure are different from Figure 3.7 as per the references used.

At the Wits Mössbauer Laboratory, CEMS is arranged as shown in Figure 3.13. The PPAD was connected to a brass cylindrical container filled with acetone at a pressure of about 20 mbar as shown in the Figure 3.13 below. An array of lead blocks was placed around the experimental setup for radiation protection to shield 80% to 90% of γ-rays emitted from the source. The estimated activity of the source was approximately 20 mCi, and the distance of 20±1 mm was maintained between the source and detector (PPAD).

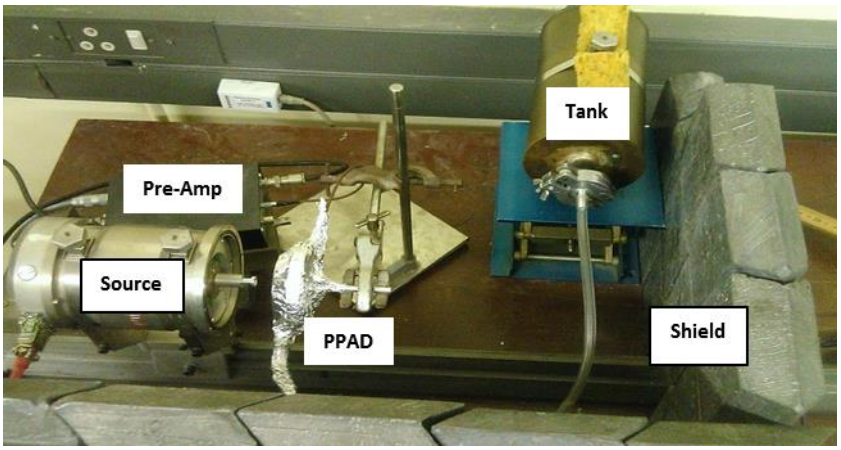

Figure 3.13: CEMS Arrangement at Wits Laboratory.

3.2.4.4. Procedures of operation in CEMS

1. The sample to be investigated was placed in the graphite conducting region of one perspex plate then mounted thereafter closed using the two compartments as shown in Figure 3.14 below.

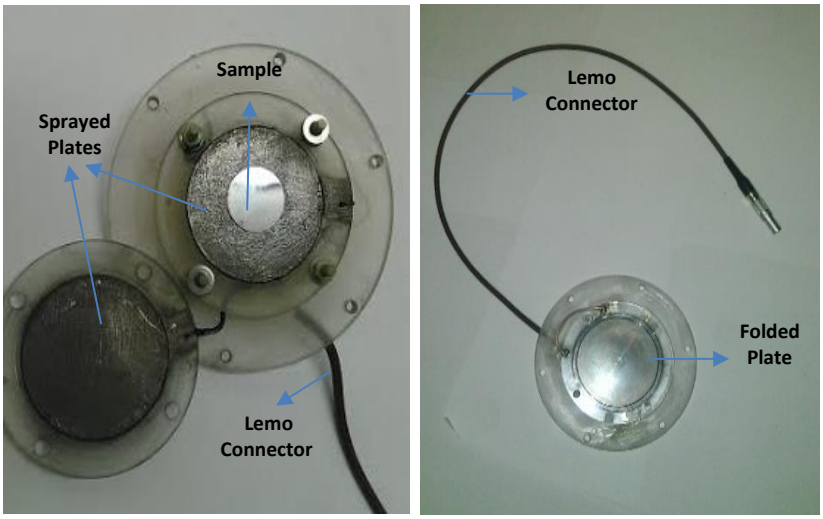

Figure 3.14: Sample mounted in PPAD.

2. The detector was then connected to the tank as illustrated in the Figure 3.15 below.

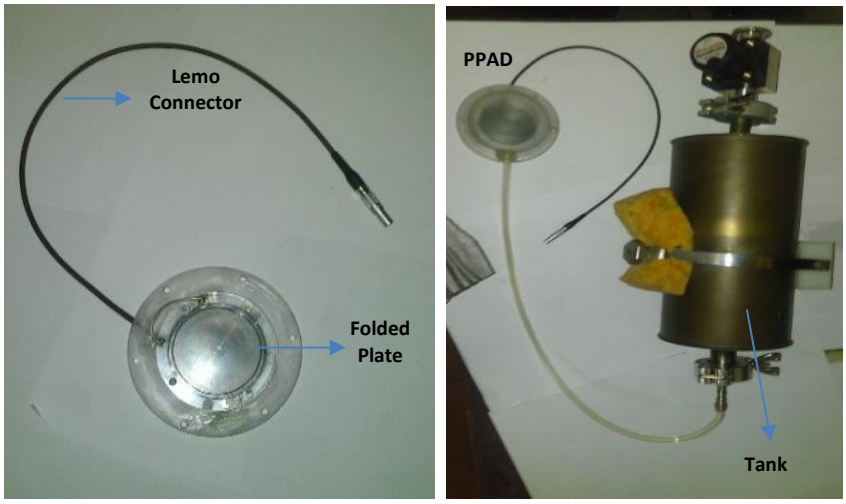

Figure 3.15: Connection of PPAD with tank.

3. Thereafter the necessary connections were made between the tank, PPAD, the vacuum pump and the flask containing the acetone as shown in the Figure 3.16.

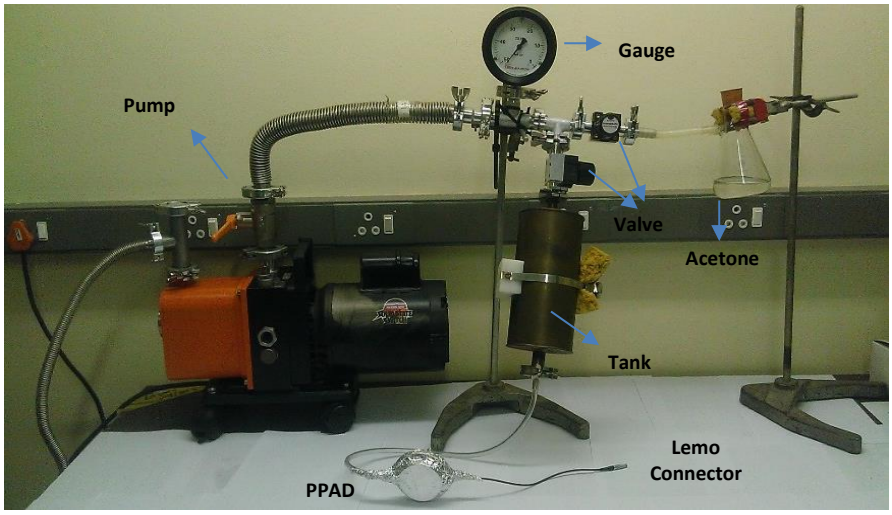

Figure 3.16: Vacuum pump station at the WITS Mössbauer Laboratory.

4. After a sequence and repetition of pumping procedures using the vacuum pump and valves, the desired pressure of between 20 mbar to 25 mbar acetone vapor was contained in the tank/PPAD. The aluminum foil was used to minimize the noise during the measurement.

3.2.4.5. Instrumentation in Mössbauer spectroscopy

The experiment set-up and instrumentation for CEMS is illustrated in Figure 3.17 comprising of a detector, source and necessary electronics.

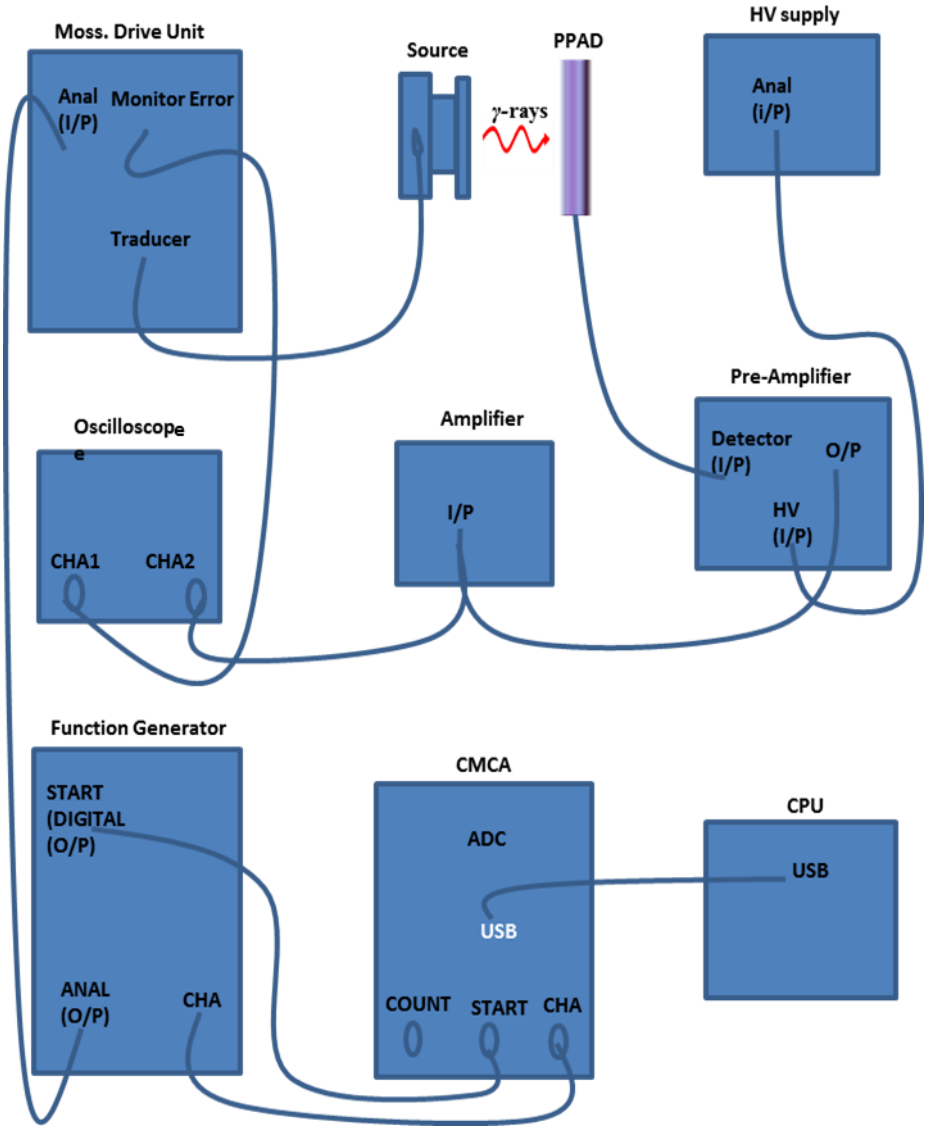

Figure 3.17: Set-up of the instrumentation used conversion electron Mössbauer spectroscopy.

The parallel-plates in the detector are connected to high voltage (HV) supply through the pre-amplifier, the pulse from the detector is firstly pre-amplified before it goes to the amplifier. Thereafter the signal is sent to a single channel analyser (SCA) which serves to reject most of the non-resonant background radiation, and to retain the pulse corresponding to 14.41 keV Mössbauer gamma rays [68]. Finally, the pulses are fed through a Multi-Channel Analyser (MCA) which operates in two modes: pulse height analysis (PHA) and multi-channel scaling (MCS). In this stage, the PHA mode is used to observe the total energy spectrum of the radiation source

and allows for the selection of only the 14.41 keV line i.e. only analyses the input pulse coincident with the logic pulse from the SCA. The MCS mode, by synchronising the channels (512) with the velocity of the Mössbauer Drive Unit passed through the Function Generator (FG), produces the reference signal which can be determined from the waveform of the Co-57 source [70]. Once the data acquisition is changed to the MSC mode, the measurement commenced which produces a histogram plotting intensity of count versus the velocity of the Co-57 source. The electronics used in CEMS is very similar to that of TMS as presented in the Figure 3.17.

3.2.4.6. Calibration of Mössbauer spectra

In this study, α-Fe foil was used for calibration at room temperature. The data was collected for a period of 12 hours. The foil is characterized as follows: 99.99% Fe, impurity of 0.01% of carbon and thickness of 12±1 μm. The theoretical hyperfine values for the magnetic field is 32.9 T with isomer shift and quadrupole splitting values corresponding to 0 mm/s [71].

Figure 3.18 depicts the velocity profile of the source recorded during single time as the MCA receives a "start" pulse from the function generator (FG). First the MCA opens channels when the source velocity passed through the negative to positive velocity by recording a value of about 512 channels as shown in Figure 3.19.

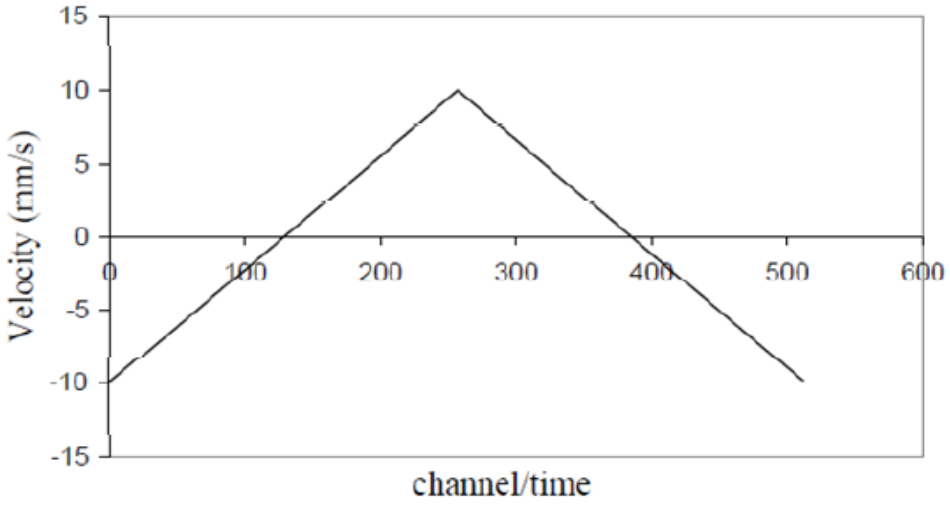

Figure 3.18: Triangular velocity profile as function of number of channels [44].

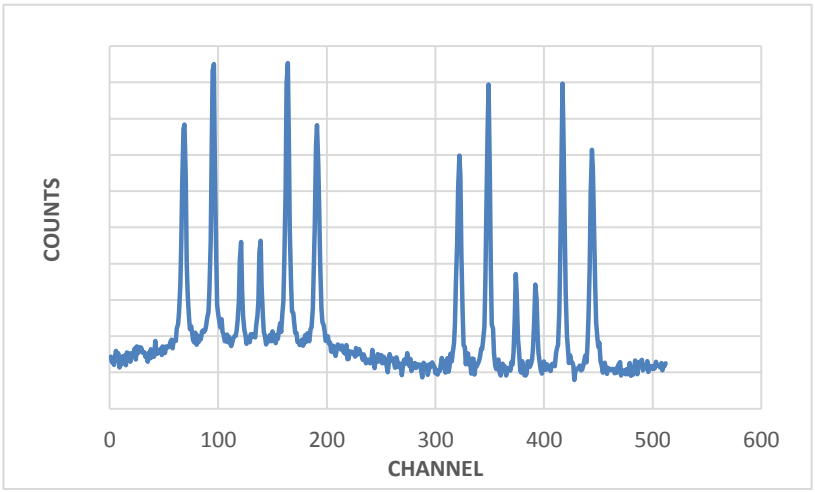

Figure 3.19: Unfolded CEM spectrum corresponding to an α-Fe foil.

The spectrum was added then folded so that the total number of channels reduced to 256 thus eliminating statistical noise. The centre of the folded Mössbauer spectrum corresponds to zero. The middle point was recorded at constant acceleration mode with a triangular wave form. Therefore, the remaining operation is to transform the velocity of the source. The calibration spectra were recorded to optimize the system so that the zero velocity and the calibration constant can be determined in order to fold the spectra.

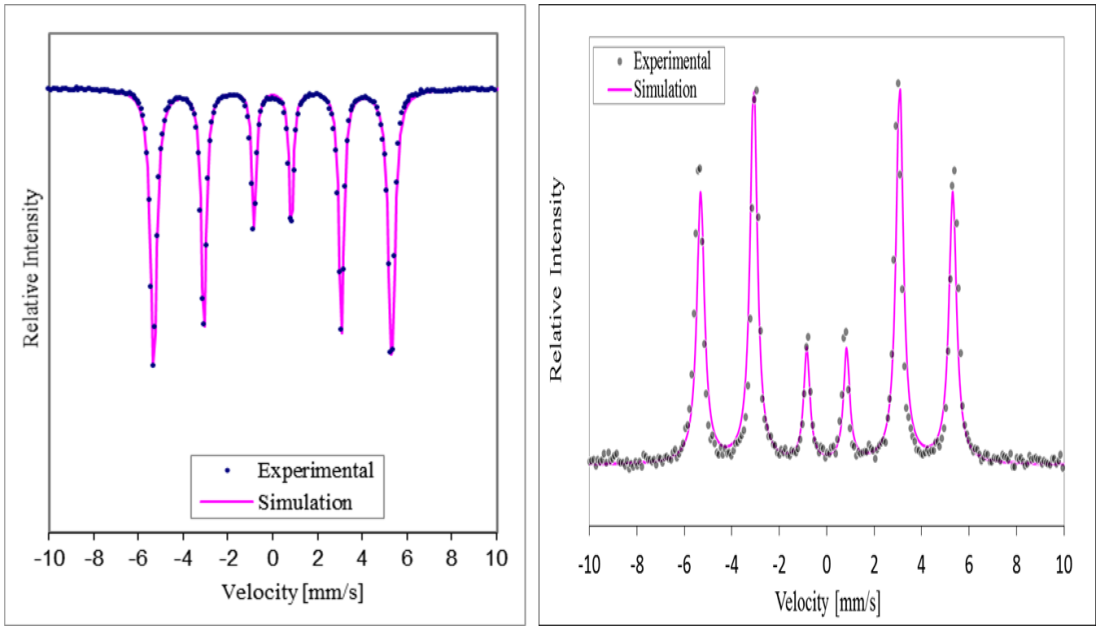

Figure 3.20: Folded Mössbauer spectrum of α-Fe foil from TMS (left) and CEMS (right).

The experimental data collected from TMS and CEMS measurements were analysed using a software package called Vinda, which is a Toolbox and is operated in a Microsoft Excel environment where all the commands are contained in a Toolbar that runs visual basic for application macros [72]. Appendix A gives more details of the fitting procedures applied in Vinda.

Chapter 4

Results and Discussion

This chapter focuses on the analysis and interpretation of data obtained from scanning electron microscopy, Energy dispersive X-ray spectroscopy, Vickers hardness, X-ray Diffraction, strain analysis and Mössbauer spectroscopy measurements. The analysis procedures, synthesis and interpretation of the results are discussed in detail. The samples investigated were powder and sintered WC-Co-TiC referred to as sample A and WC-Co-TiC-Fe represented as sample B.

4.1. Vickers hardness measurements

The Vickers hardness values for samples A and B were obtained using the Vickers Hardness test. The data was acquired at five different spot areas on each of the as-sintered samples A and B. The error values were determined from the standard deviation calculation of the five measured values. Table 4.1 gives the Vickers hardness results for both samples.

Table 4.1: Vickers hardness results of the as-sintered samples A and B.

Sample	Indention measurements values (HV)	Vickers hardness (HV)	*Hardness (MPa)
A	1360 1433 1377 1379 1244	1358±70	13316±682
B	775 855 778 846 853	820±41	8051±403

***1 HV = 9.80 MPa**

An average Vickers hardness value of 1358±70 HV was determined for sample A and a value of 820±41 HV was obtained for sample B. Bhaumik *et al.* [24] found the Vickers hardness values of 1370 HV and 1395 HV for WC-10Co and WC-10Co-12TiC, respectively which are compared with the hardness of the as-sintered samples as illustrated by the histogram in Figure 4.1.

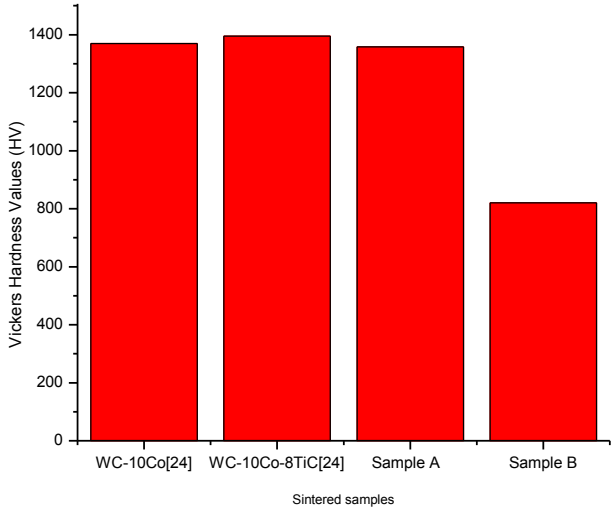

Figure 4.1: Histogram showing the Vickers hardness for the as-sintered samples A and B compared with WC-10Co reported by Bhaumik *et al.* [24] .

The addition of TiC as a binder to the WC-Co system increases the hardness of the WC-Co-TiC alloy as observed by Bhaumik *et al*. [24]. The Vickers hardness value of 1358 HV obtained for sample A (WC-10Co-6TiC) also compares well with the values of 1370 HV and 1395 HV reported by Upadhaya [25] for WC-8TiC-12Co. The small difference in values could be due to the size and the weight percentage of the individual starting materials. However, in our study, the increase in volume of the binder, and the presence of iron in the as-sintered sample B (WC-10Co-6TiC-Fe) reduces the hardness value by 36% compared to the as-sintered sample A. The lower hardness value for WC-10Co-6TiC-20Fe is due to the increase in wt% of the binder content compared to the WC-10Co-6TiC sample where the wt% of the binder material is 16%. The WC grain size was similar for both materials (WC-10Co-6TiC and WC-10Co-6TiC-20Fe), thus eliminating the effect of the WC grain size on the hardness values. The SEM micrograph shown later revealed that sample A contained similarly sized WC grains, while those in sample B are more varied in size. This difference in grain size has direct bearing on the hardness of the sample.

In sample B, titanium carbide and cobalt increases the hardness value of the sample compared to the result found by Brayner [73] for WC-Fe. For the WC-Fe system, the

hardness value of 756 HV was determined in the absence of Ru in this sample. It is be clear that TiC and Co decreases the hardness of the WC system compared to the value of 1814 HV for the WC-Fe obtained by Han *et al.* [26]. The large difference has been attributed to the size of the WC and Fe particles.

4.2. Microstructure measurements

Elemental analysis of the as-sintered samples was conducted using scanning electron microscopy (SEM). The SEM system was operated at a voltage of 20 kV equipped to an energy dispersive X-ray detector.

Figure 4.2 depicts the SEM micrograph of the as-sintered samples A and B which were collected in the backscattered electron mode (BSE) at a magnification of 5000.

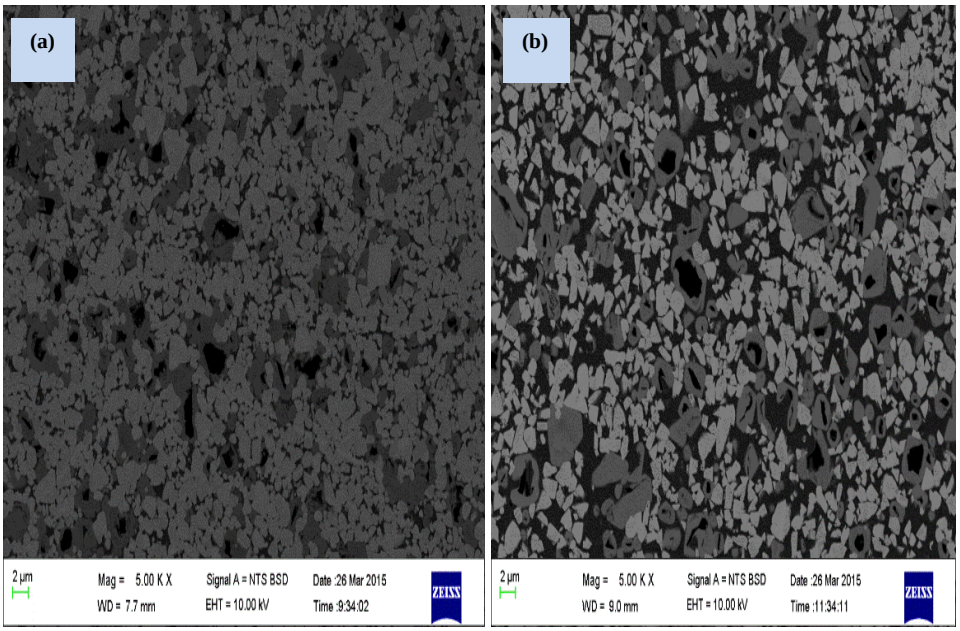

Figure 4.2: (a) SEM-BSE image for the as-sintered sample A and (b) SEM-BSE image for the as-sintered sample B recorded with magnification of 5000.

In Figure 4.2 (a), the light areas represent the WC regions whilst the darker regions indicated the presence of Ti, C and Co elements. The light areas in Figure 4.2 (b), also represent the WC regions whilst the dark regions are dominated by the binder elements Ti, C, Co and Fe.

Figure 4.3 shows the SEM micrograph of both the as-sintered samples A and B which were collected in the backscattered electron mode (BSE) at a magnification of 20000.

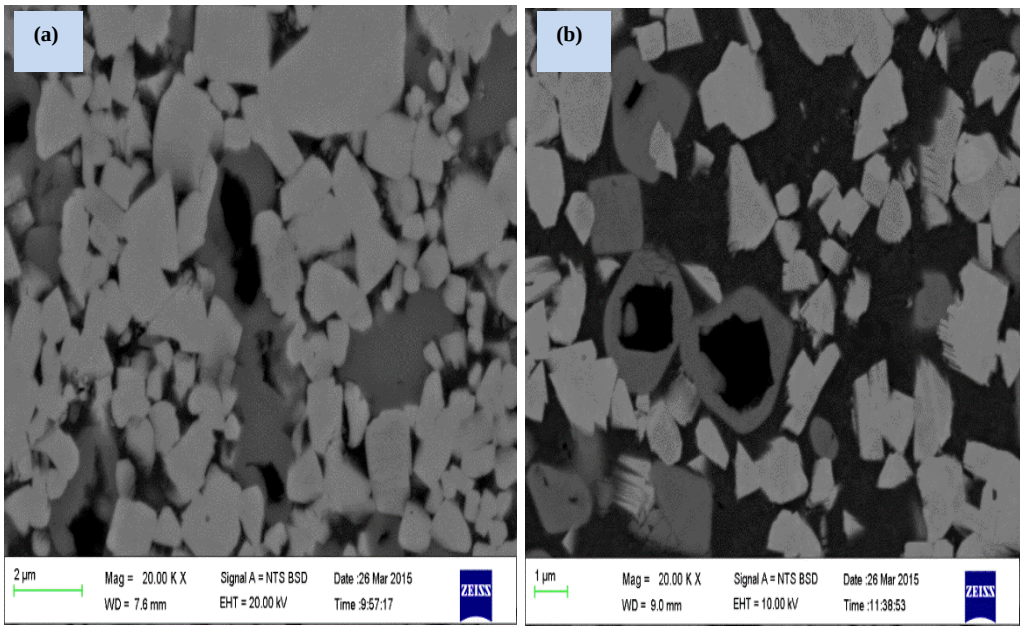

Figure 4.3: (a) SEM images for the as-sintered A and (b) the as-sintered sample B at a magnification of 20000.

These images show the expanded view of the light and dark regions in the as-sintered samples A and B since the Figure 4.3 (a) and (b) were obtained at a high magnification.

Figure 4.4 (a) depicts the SEM micrograph of the as-sintered sample A while the associated EDS spectrum with the elemental composition of the material is shown in Figure 4.4 (b).

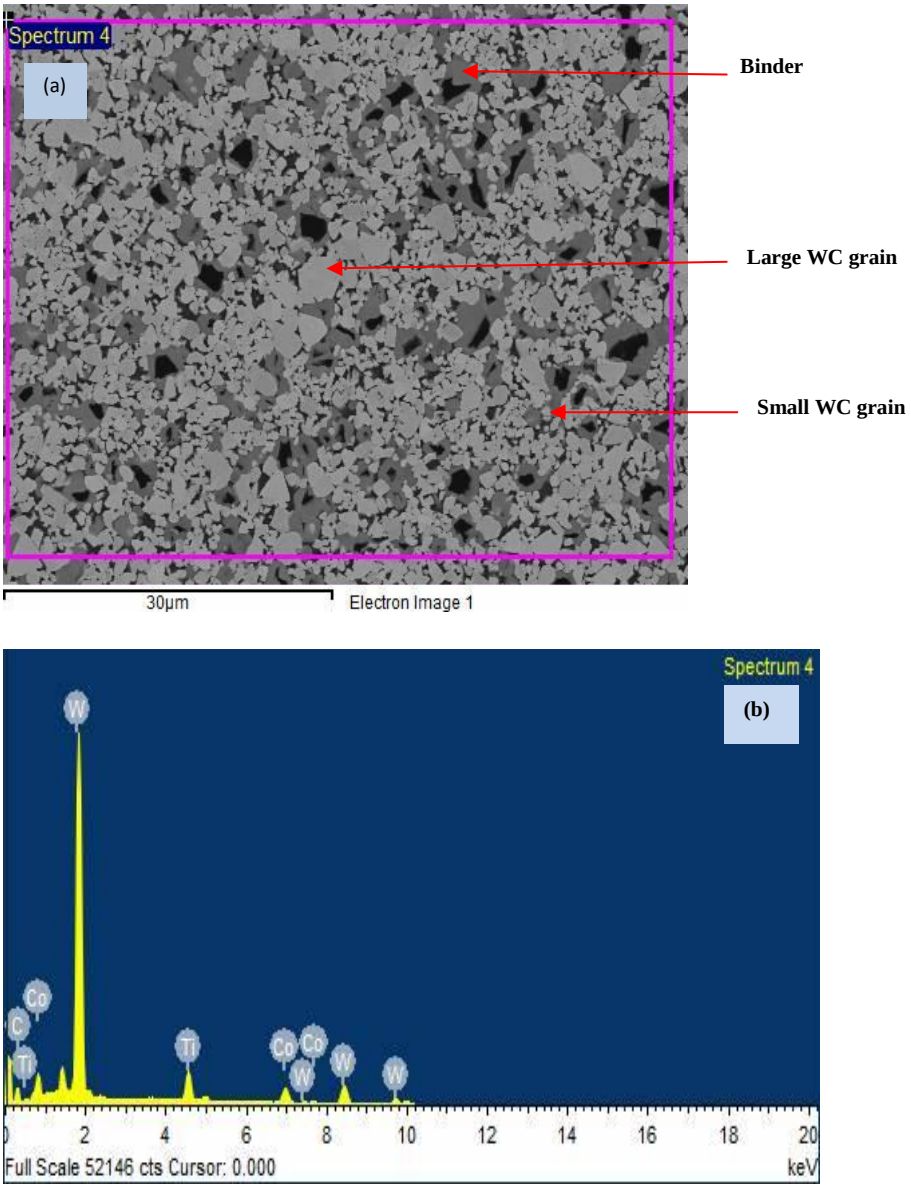

Figure 4.4: **(a) SEM micrograph on the overall average composition and (b) the EDS spectrum showing the composition of elements present in the as-sintered sample A.**

The microscopy result in Figure 4.4 (a) shows large irregular shaped WC grains with diameters ranging from 2 µm to 8 µm which are randomly dispersed. The binder microstructures are not homogenous. The EDS analysis in the Figure 4.4 (b) reveals that the as-sintered sample A contains the following elements: W, C, Co and Ti.

Figure 4.5 (a) shows the SEM backscattered electron (BSE) micrograph of the as-sintered sample A with the EDS spectrum 2 on the matrix area.

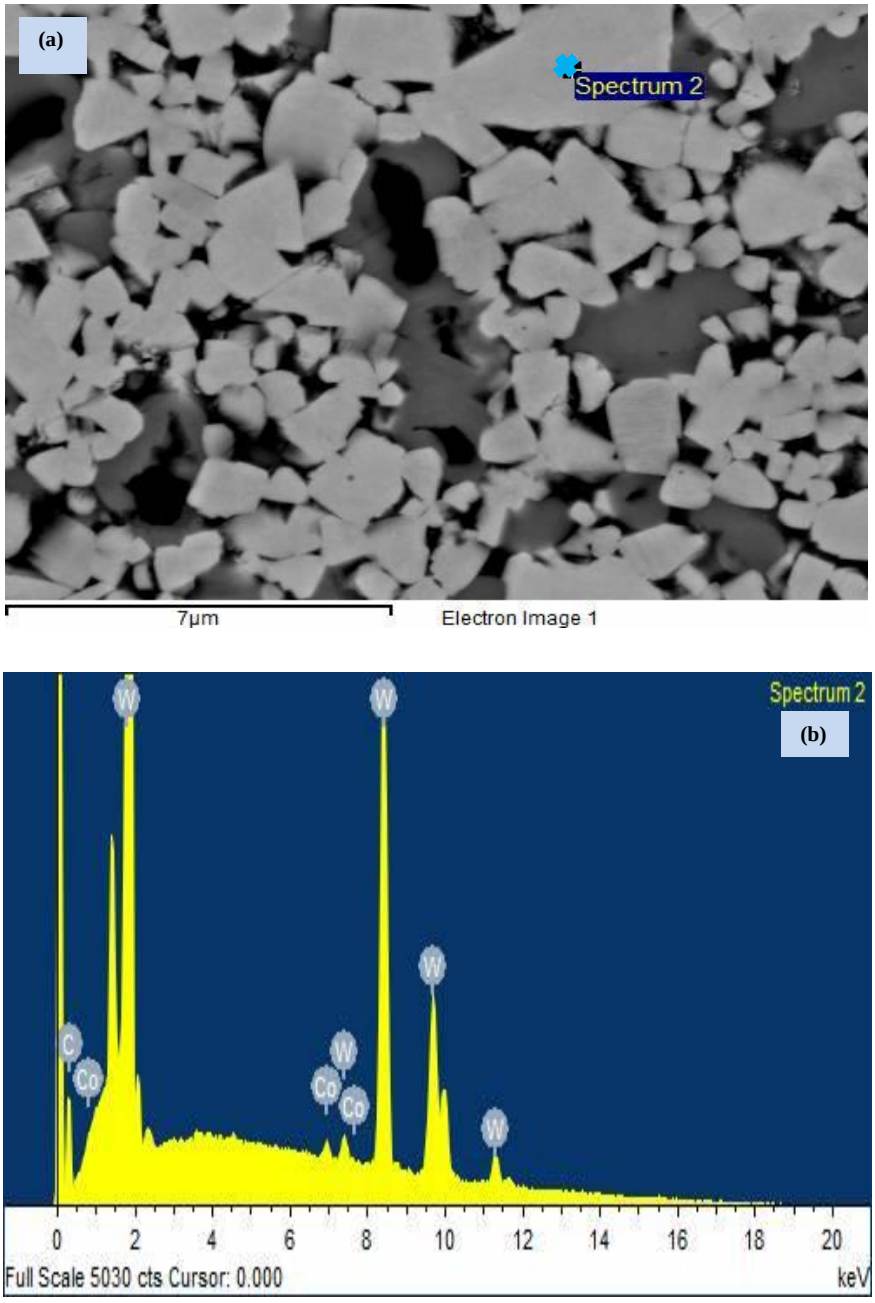

Figure 4.5: (a) SEM-BSE micrograph on the light region and (b) spectrum 2 on the EDS micrograph showing the composition of elements present in the as-sintered sample A.

Figure 4.5 (b) shows the elemental composition at light region. The composition on the blue marker denoted by a cross is dominated by the presence of tungsten. No titanium is present in the EDS results obtained at the light region.

The SEM-BSE micrograph of the as-sintered sample B with the associated EDS spectrum on the overall micrograph is presented in Figure 4.6. The microstructure

results show large irregular shaped WC grains with diameters ranging from 0.5 µm to 3 µm which are randomly dispersed and closely packed. The binder microstructures are not homogenous.

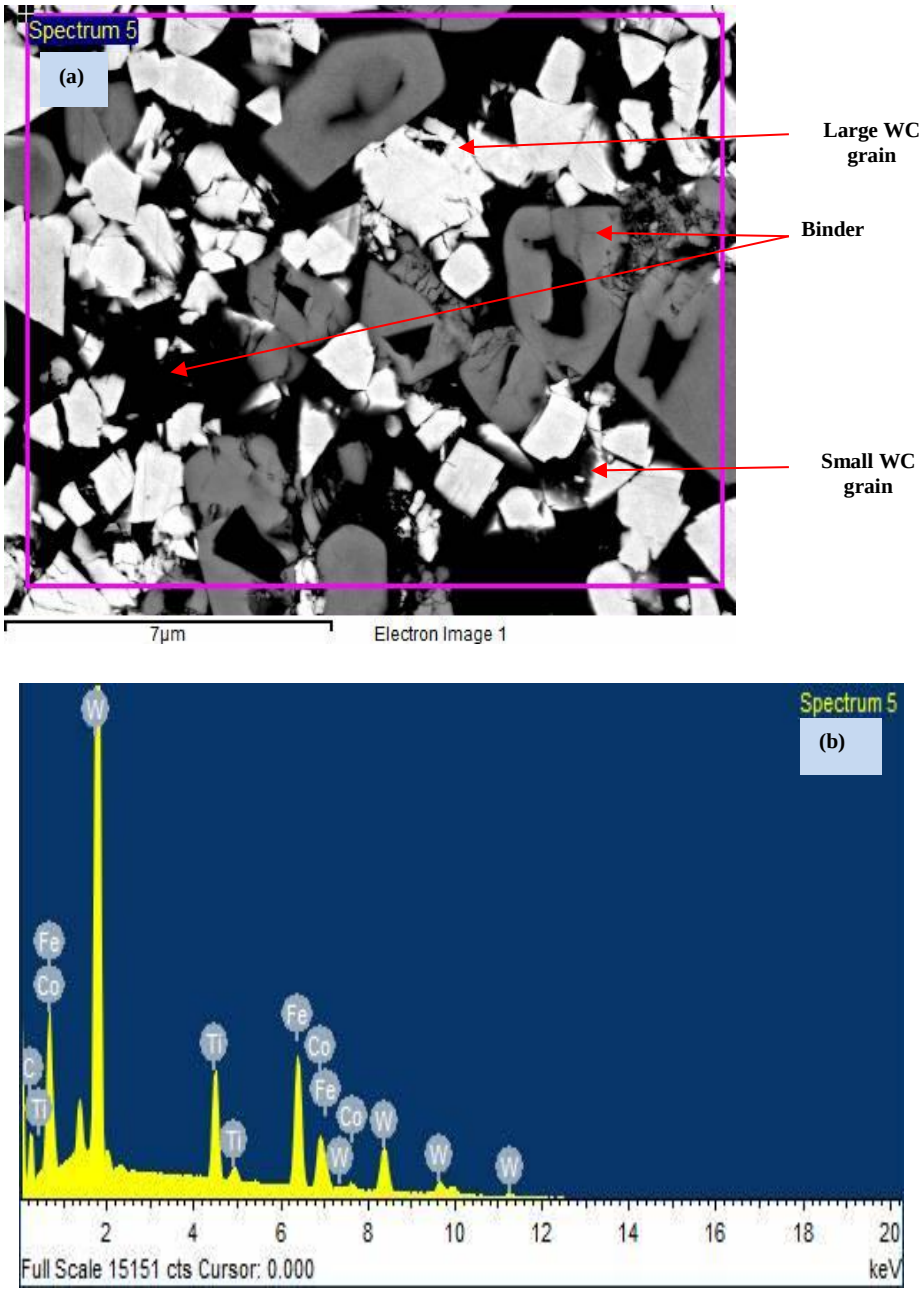

Figure 4.6: (a) SEM-BSE micrograph on the overall average and (b) the spectrum of elements present in the as-sintered sample B.

Figure 4.7 shows the SEM-BSE micrograph of the as-sintered sample B with the EDS spectrum 3 recorded on the light region showing the different elements of the binder phase.

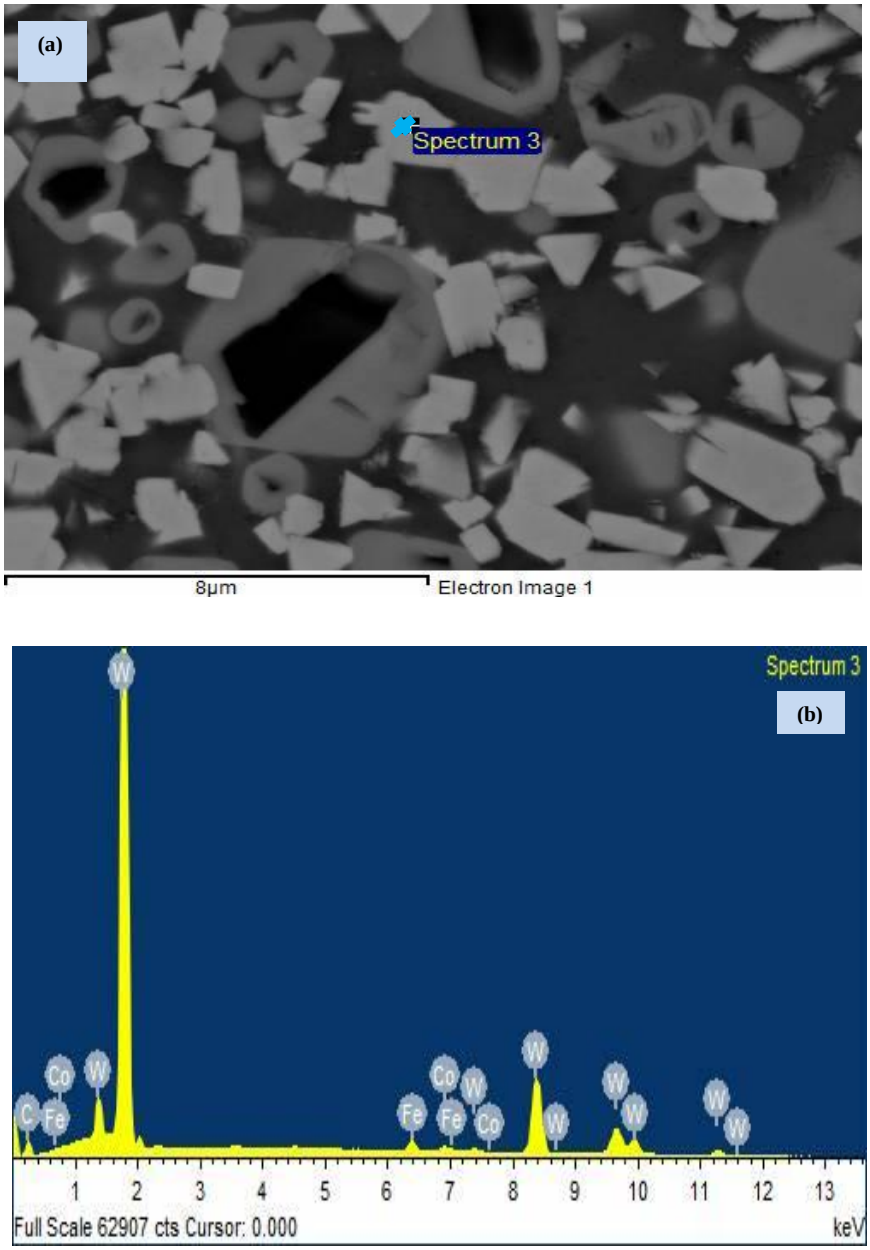

Figure 4.7: (a) SEM-BSE micrograph of the as-sintered sample B and (b) spectrum 3 recorded on the light region showing the composition of elements present in the sample.

The Fe content features as the darker binder regions in the BSE microgram while regions with higher tungsten content appears in the lighter regions. This is due to

the higher average atomic number of tungsten compared to carbon. These results are consistent with the SEM data on WC-Co reported by Varacalle *et al.* [74] and Guilemay *et al.* [75] who observed tungsten carbide (WC) in light regions of the micrograph whilst cobalt (Co) was identified in dark regions and W_2C phases appear to be in lighter regions than WC.

The SEM-BSE images of samples A and B show the presence of some holes in the sample which are most likely attributed to the removal of carbide particle grains during the polishing process. The different morphologies of grains is due to the orientation of each grain when the electron beam interacted with the specimen surface. In addition, the differing morphologies could also be caused by the sintering process where variation of the physico-chemical parameters (temperature, pressure, volume etc.) have direct effects on the grain during sintering process.

4.3. X-ray Diffraction measurements

XRD measurements were conducted using a Bruker D2 Phaser associated with a LynxEye detector. The XRD patterns for samples A and B were collected over a 2θ range of 20° to 100° for 10 minutes. These results are shown in Figures 4.12 and 4.13. Figure 4.12 displays the XRD patterns obtained for the as-milled powder and as-sintered samples A.

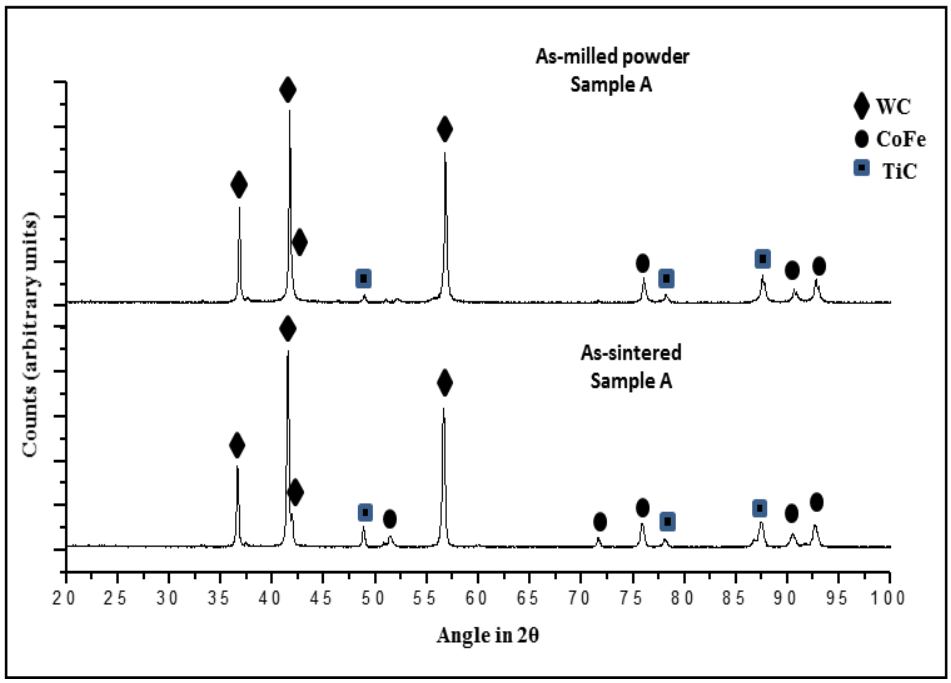

Figure 4.12: Fingerprint pattern obtained for the as-milled powder and as-sintered samples A.

The patterns indicate the presence of WC, TiC and CoFe phases with different abundances. The result shows the formation of CoFe phase induced by the milling process of the starting materials after the samples were milled for 15 hours. Akkouche *et al.* [39] performed an XRD measurement on a nanocrystalline $Fe_{50}Co_{50}$ powder sample [39] and reported the preferential formation of CoFe after 43 hours of milling time.

The fingerprint pattern confirms that the TiC and FeCo phases are face centered cubic with lattice parameters, $a = b = c = 4.32$ Å and $a = b = c = 3.54$ Å, respectively. The WC phase is hexagonal with lattice parameters, $a = b = 2.90$ Å and $c = 2.84$ Å with $\alpha = \beta = 90°$ and $\gamma = 120°$.

Figure 4.13 illustrates the XRD pattern for the as-milled powder and as-sintered sample B. This pattern indicates the presence of WC, TiC, CoFe and Co phases with different percentages.

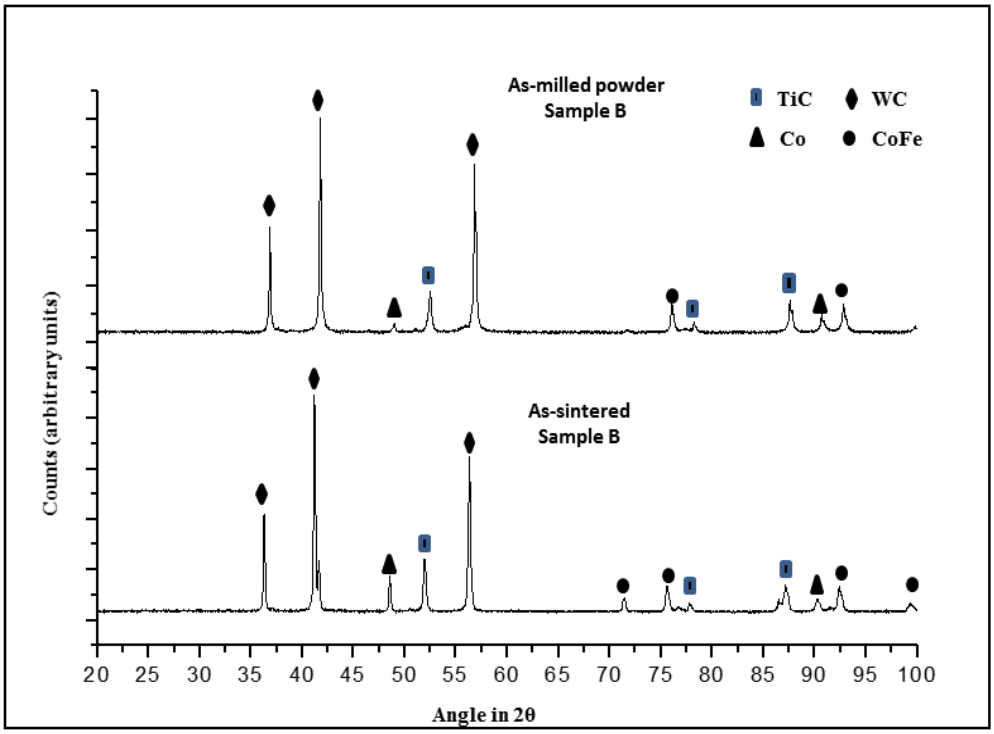

Figure 4.13: Fingerprint pattern obtained for the as-milled powder and as-sintered samples B.

The fingerprint pattern results show that there is formation of the CoFe phase with cubic crystal structure and lattice parameters of $a = b = c = 2.86$ Å. All the peaks are allocated in the range of 50°–100° (2θ). This result is in agreement with Sorescu *et al.* [38] who investigated the magnetic and structural properties of the $Fe_{50}Co_{50}$ system and reported that the peaks corresponding to the FeCo phase appeared between 50° 100° (2θ) and all the cobalt peaks were dissolved in bcc-Fe forming the new CoFe phase. The WC phase is hexagonal with lattice parameters, $a = b = 2.90$ Å and $c = 2.84$ Å with $\alpha = \beta = 90°$ and $\gamma = 120°$. The TiC and Co persists as face-centered cubic in the samples understudy.

4.4. Strain analysis

The strain results were obtained from the XRD patterns in Figure 4.12 and 4.13 by adopting the method used in accordance with the Topas description defined in the Topas manual (v4-2) and that of other research [67, 76]. To this effect a preliminary (prior to treatment) sample is used for a description of the peak shape from the sample and

instrumental contributions. These contribute to the peak shift of the diffractogram resulting from the instrumental components and any operating conditions. The derived analytical values were then used for the strain analysis of the treated sample. The analysis is of the strain value and not of the stress tensors. In this study, the as-milled samples represent ‘‘prior to treatment’’ and the as-sintered represent ‘‘the treated samples’’. The relative strain results were determined from the diffractograms for the “prior and treated samples” using the broadening of the spectral lines.

Figures 4.16 and 4.17 show the Rietveld analysis including the phases obtained on the as-milled powder and as-sintered samples A, respectively from which the strain results were extracted. In the legend, the different colours represent the different phases which are specified at the bottom of the X-ray pattern.

In Figures 4.16 to 4.19 the solid red line indicates the simulation whilst the experiment data represented by the blue solid line. The solid line below the graph shows the error in the fits. The Rietveld analysis gives the phase analysis for the as-milled powder sample A as shown in Figure 4.16 as WC (56%), CoFe (36%) and TiC (8%). The legend in Figure 4.16 - 4.19 is as explained above.

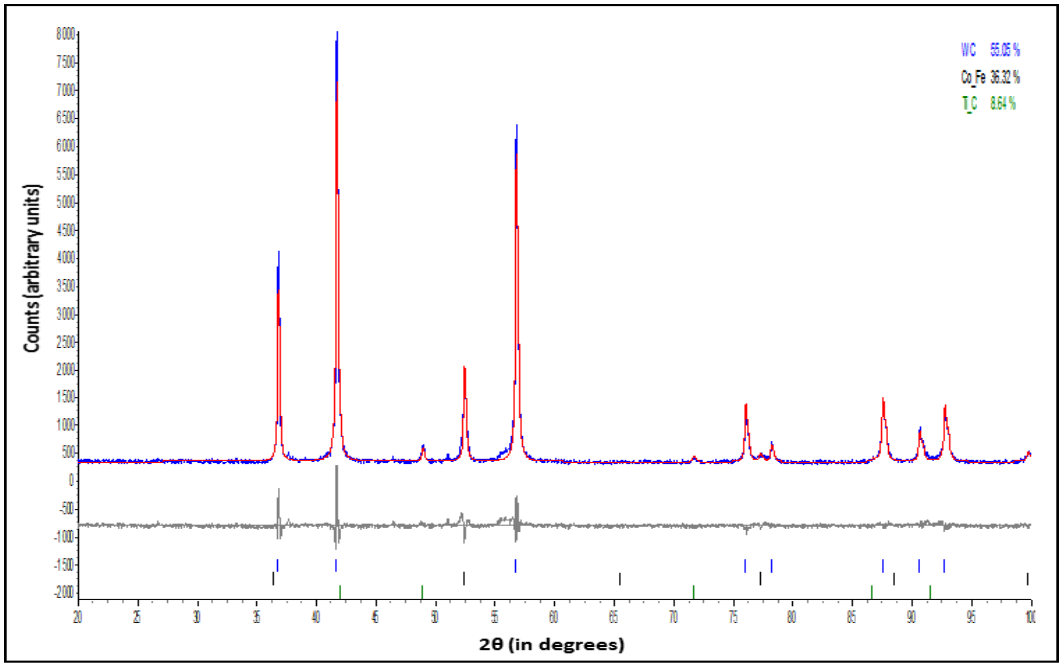

Figure 4.16: Rietveld analysis for the as-milled powder sample A.

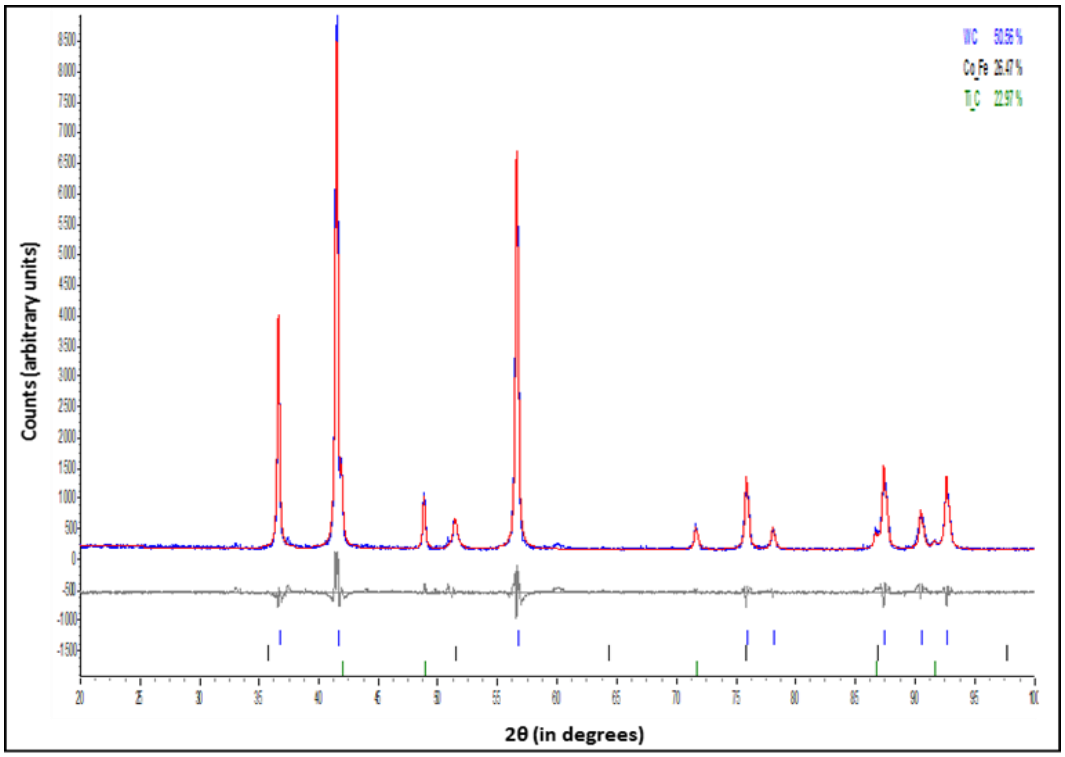

Figure 4.17: Rietveld analysis for the as-sintered sample A.

For sample A, the tungsten carbide phase appears to have little strain whilst the titanium carbide phase appears to have no strain. The cobalt iron phase, however, appears to have strain associated with it. The strain ratio is the change in strain between the as-milled and the as-sintered samples A and may not represent an absolute value as illustrated in the Table 4.2.

Table 4.2: Strain ratio of the phases determined for the sintered sample A.

Phase	WC	CoFe	TiC
Strain Ratio	4.04×10^{-5}	8.00×10^{-4}	2.18×10^{-7}

Figures 4.18 and 4.19 show the XRD patterns including the respective phases for the as-milled powder and the as-sintered samples B from which the strain results were extracted.

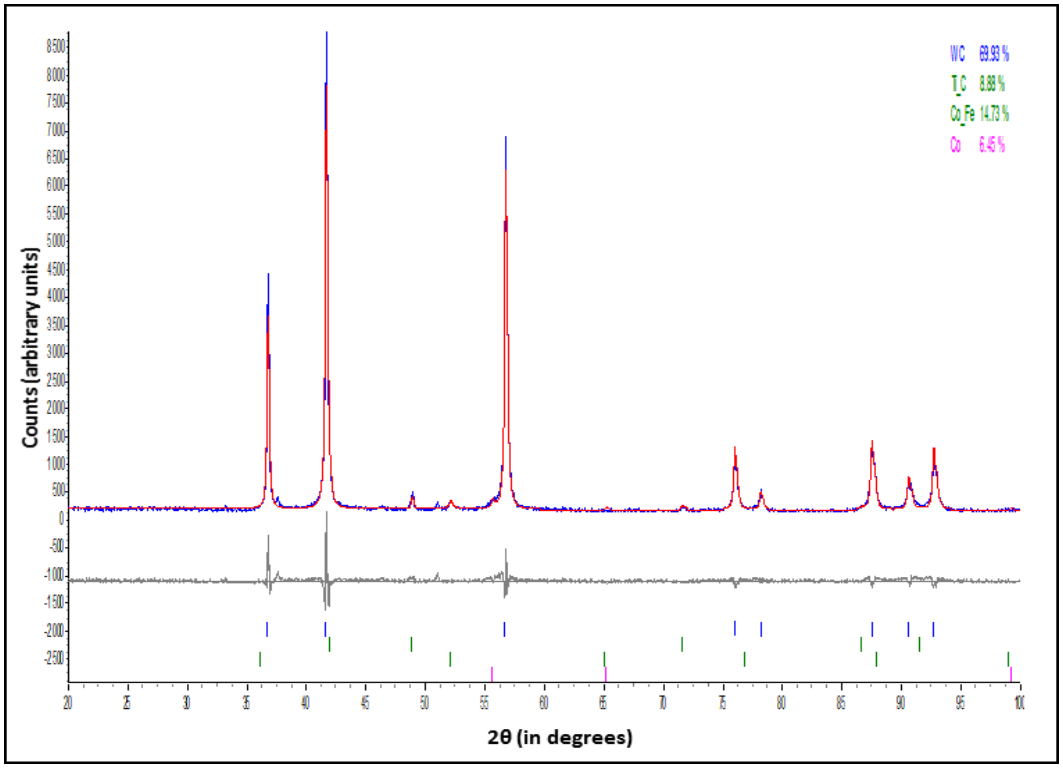

Figure 4.18: Rietveld analysis for the as-milled powder sample B.

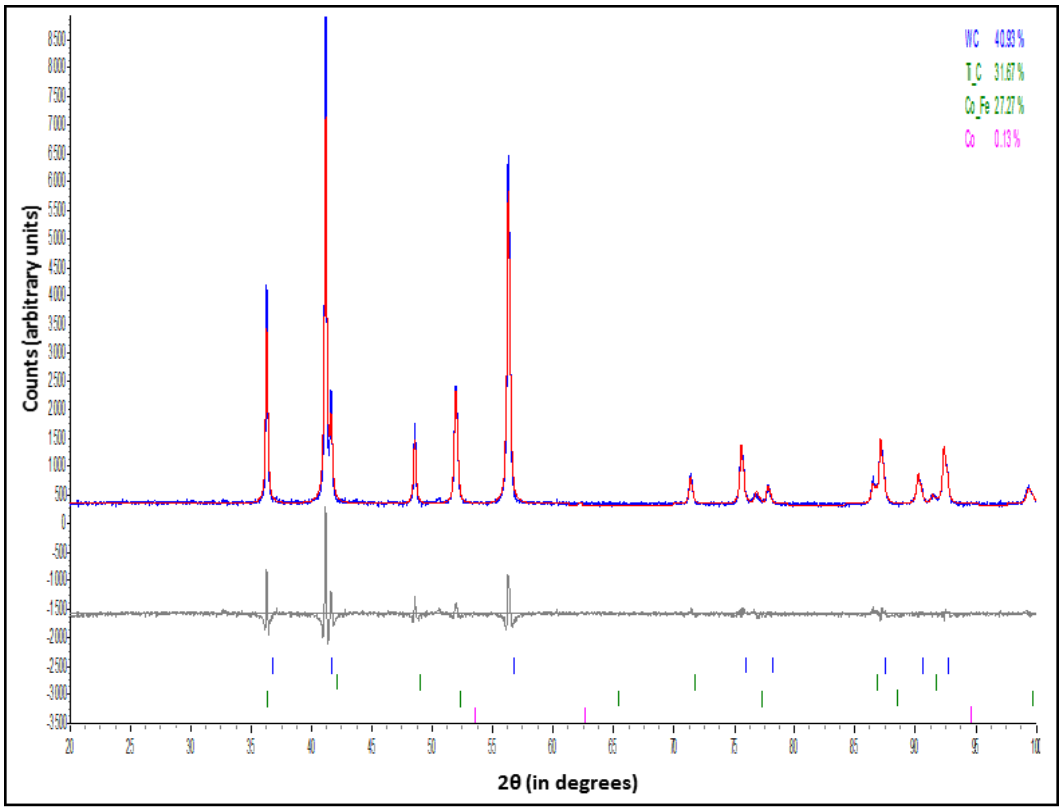

Figure 4.19: Rietveld analysis for the as-sintered sample B.

All phases show no significant strain however it appears that the crystallites have either reduced their strain during treatment or the average crystallite domain size has increased. The strain ratio determined is the change in strain between the pre and post treated samples B and may not represent an absolute value as shown in Table 4.3.

Table 4.3: Strain ratio of the phases extracted for the sintered sample B.

Phase	WC	CoFe	TiC	Co
Strain Ratio	2.18×10^{-7}	2.18×10^{-7}	2.18×10^{-7}	2.18×10^{-7}

4.5. Mössbauer spectroscopy results

This section describes the Mössbauer spectroscopy studies undertaken on the WC-Co-TiC-Fe sample. A transmission Mössbauer spectroscopy (TMS) measurement was done on the powder sample and a conversion electron Mössbauer spectroscopy (CEMS) measurement was conducted on the as-sintered sample. A ^{57}Co radioactive source with an activity of 20 mCi was used in these experiments. The data from the TMS and CEMS measurements were collected within a month, resulting in spectra with good statistics required to perform meaningful data analysis.

4.5.1. Analysis Procedure

The analysis of the TMS and CEMS data was carried out using Vinda, a spreadsheet base code built on Visual Basic for Applications developed by Gunnlaugsson [71]. The observed transmission Mössbauer spectrum was analysed using the Lorentzian line shape. Only one sextet required to give good fits to the data. Similarly, the CEMS results also showed a sextet like feature which was also analysed with Lorentzian lineshape comprising of two sextets, one doublet and one singlet. All measurements were performed at room temperature.

4.5.2. TMS calibration spectrum

Figure 4.18 gives the Mössbauer spectrum for α-Fe foil collected at room temperature for approximately 10 hours. The foil is characterized as follows: 99.99% Fe and impurity of 0.01% of carbon and thickness of 12±1 μm. The calibrations were done to optimize the system in order to determine the zero velocity.

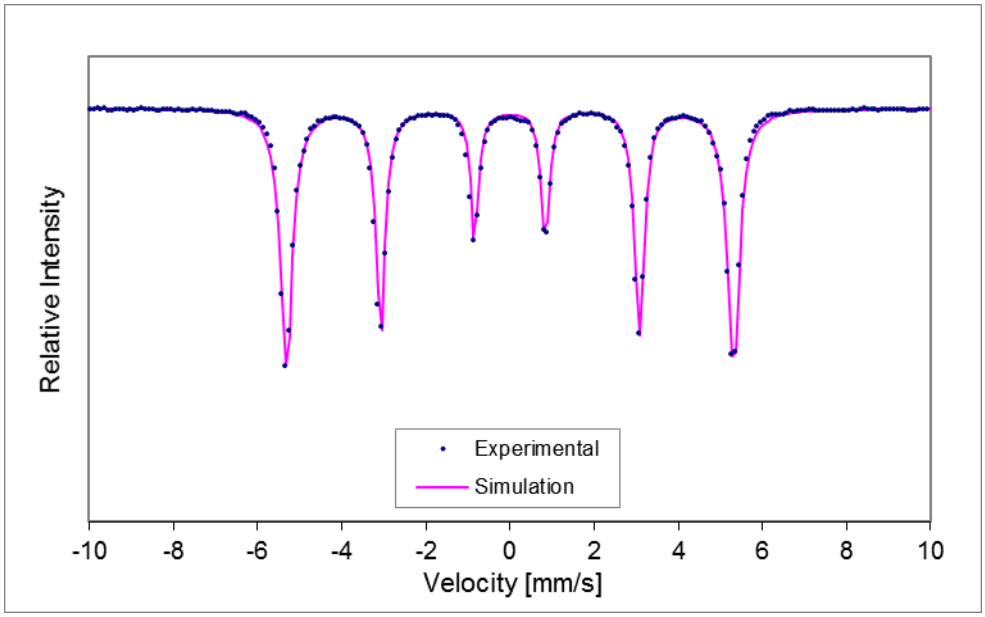

Figure 4.18: Folded Mössbauer spectrum for α-Fe foil.

The hyperfine parameters obtained from the data analysis for the α-Fe foil are presented as follows: the hyperfine magnetic field, B_{hf} = 32.9 T, isomer shift (δ) and quadrupole splitting (ΔE_Q) values of 0 mm/s. These results are in good agreement with the calculated hyperfine values of B_{hf} = 33.2 T, δ and ΔE_Q values corresponding to 0 mm/s [71].

4.5.3. TMS spectrum for the powder sample

Figure 4.19 shows the Mössbauer spectrum for the as-milled powder WC-Co-TiC-Fe sample measured at room temperature. The data was collected for a period of 72 hours.

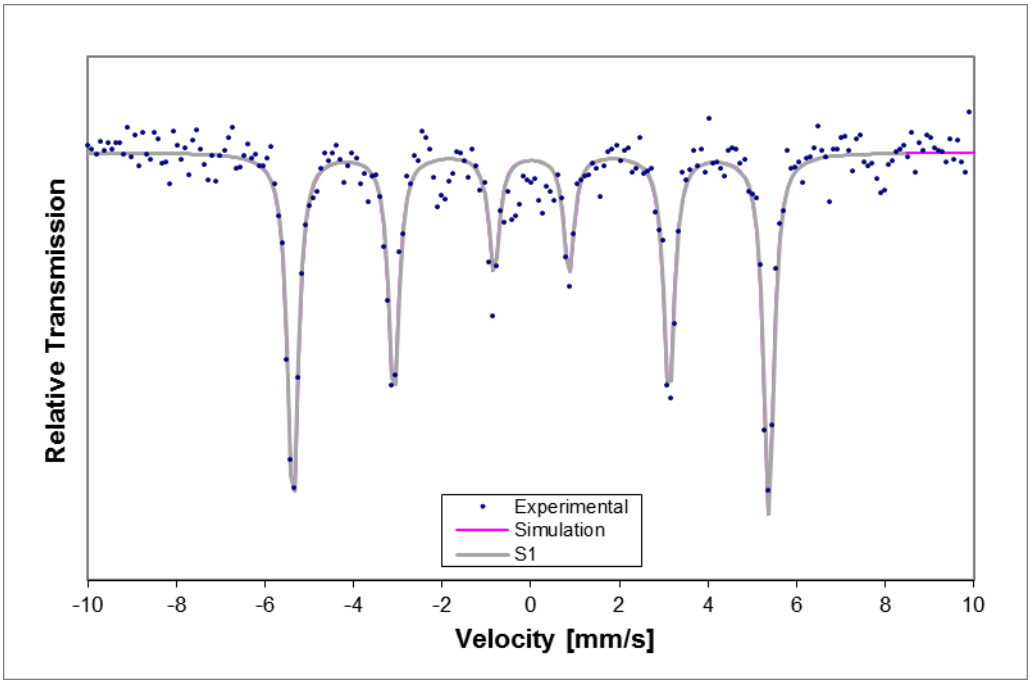

Figure 4.19: Mössbauer spectrum for the as-milled powder WC-Co-TiC-Fe obtained at room temperature.

The spectrum was fitted with one sextet component. The hyperfine parameters extracted from the data analysis for the powder sample are presented in the Table 4.4. The isomer shift values are reported relative to α-Fe.

Table 4.4: Hyperfine parameters extracted from the fits to WC-Co-TiC-Fe data collected by TMS.

Component	δ (mm/s)	ΔE_Q (mm/s)	B_{hf} (T)	Rel. Area (%)	Γ (mm/s)
S1	0.007(3)	- 0.02(1)	33.3(3)	100	0.28

The hyperfine magnetic field of 33.3 T compares well with the calculated value [71] obtained for α-Fe foil.

This result as shown in Table 4.4 suggests that there are no chemical reactions between the constituent elements in the powder sample during the milling process. Thus, in the milling process Fe does not react with others elements in the sample [70], but does not exclude the formation of other non-Fe containing compounds or phases. This result is not in agreement with the data obtained by

Szumiata *et al.* [77] who found that after a milling time of 1 hour to 40 hours of $Fe_{50}Co_{50}$ a hyperfine magnetic parameter of approximately 34.5 T corresponded to solid bcc-FeCo which the difference is due to samples preparation of the materials.

4.5.4. CEMS calibration spectrum

Figure 4.20 shows the CEM spectrum for the α-Fe foil measured at room temperature. The spectrum was recorded with a parallel plate avalanche counter (PPAD) which was subjected to a pressure of 25 mbar and a bias voltage in the range 500 - 900 V was applied. The data were collected for a period of 34 hours to obtain good statistics.

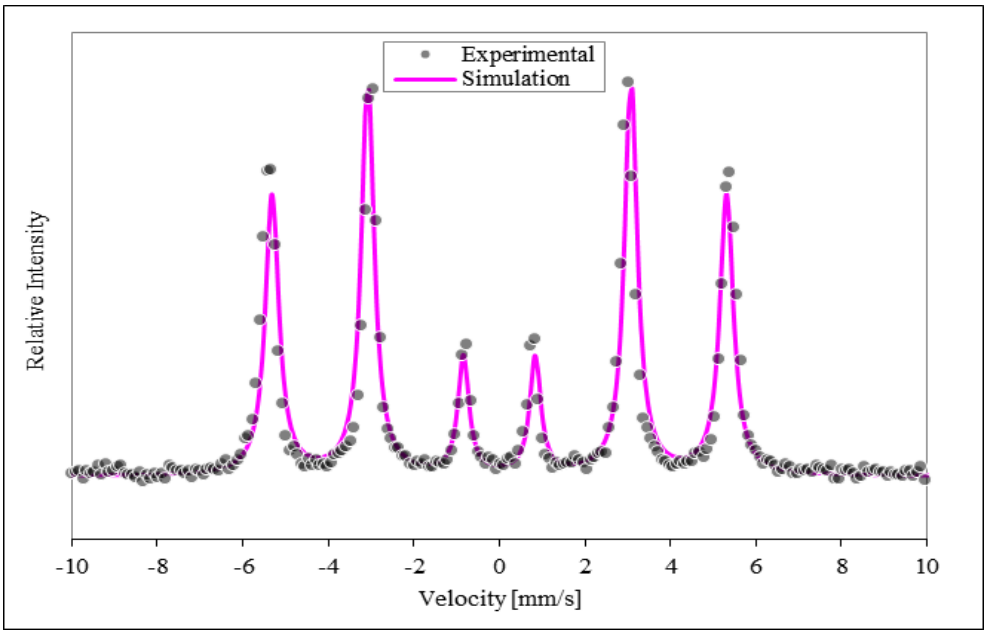

Figure 4.20: Folded CEM spectrum of the α-Fe foil.

The hyperfine parameters obtained from the CEMS data analysis of α-Fe foil are: B_{hf} = 32.9 T, δ and ΔE_Q values of 0 mm/s which compares well with the calculated hyperfine values for the hyperfine magnetic field of 33.2 T, and the respective isomer shift and quadrupole splitting values of 0 mm/s [71].

4.5.5. CEMS spectrum for the sintered sample

Figure 4.21 shows the CEMS spectrum obtained at room temperature for the sintered WC-Co-TiC-Fe sample. The data was collected for 14 days.

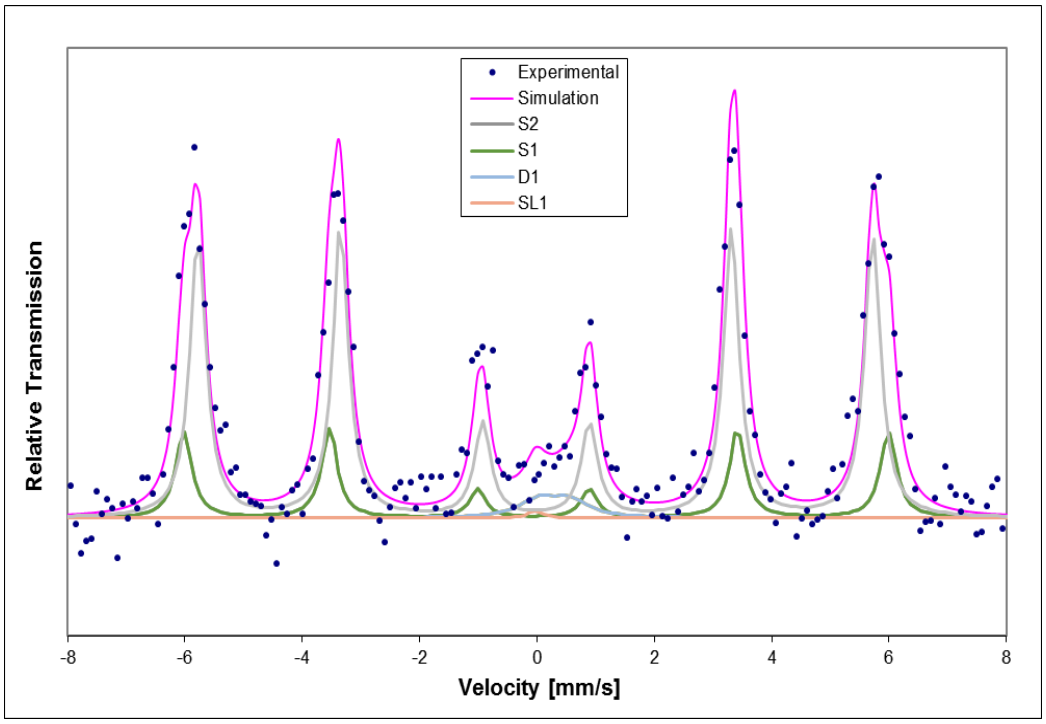

Figure 4.21: CEM spectrum for the as-sintered WC-Co-TiC-Fe sample obtained at room temperature.

The spectrum was fitted with four spectral components: two sextets labelled S1 and S2, one single line SL1 and one doublet D1. The room temperature hyperfine parameters obtained from the fits to the data for the as-sintered WC-Co-TiC-Fe sample is given in the Table 4.5.

Table 4.5: Hyperfine parameters for the WC-Co-TiC-Fe sample obtained at room temperature.

Component	δ (mm/s)	ΔE_Q (mm/s)	B_{hf} (T)	Rel. Area (%)	Γ (mm/s)
S1	- 0.04(1)	0.05(2)	37.2(1)	24	0.33
S2	- 0.02(1)	- 0.01(1)	35.6(9)	80	0.33
D1	0.28(6)	0.54(8)	-	5	0.80
SL1	0.026	-	-	1	0.33

The CEMS results reveal that the spectral components S1 and S2 are characterised by hyperfine magnetic field values of 37.2 T and 35.6 T, respectively. The B_{hf} value of 35.6 T obtained for S2 is in good agreement with the value of 35 T determined by Sorescu *et al.* [38] in their Mössbauer study of FeCo powder samples. In addition, the magnetic hyperfine parameters of S2 compares well with the result obtained by Akkouche *et al.* [39] who found that an average B_{hf} of 35 T, corresponded to the bcc crystalline structure of the FeCo solid solution. Further these results are comparable with the value of 35 T found by Moumeni *et al.* [78] for bcc-FeCo. Therefore, the spectral component S2 is attributed to FeCo. The magnetic hyperfine field of 37.2 T determined for S1 is in good agreement with the value of B_{hf} = 37 T obtained for FeCo phase as reported by Yu *et al.* [79].

The isomer shift value depends on the *s*-electron density at the Fe nucleus and increases in the isomer shift value indicates a change in the bonding mechanism of ^{57}Fe in the as-sintered sample. The large value of the isomer shift indicates that there is formation of a phase which has a lower value of electron density. The isomer shift and quadrupole splitting for spectral component D1 was determined as 0.28 mm/s and 0.54 mm/s, respectively. Tendal *et al* [5]. performed Mössbauer measurements on the FeWC compound and found isomer shift and quadrupole splitting values of 0.26 mm/s and 0.53 mm/s, respectively, which is corresponds well with the values obtained in this study. Therefore, D1 is attributed to the FeWC phase. In this study, the isomer shift of the single line SL1 component was determined as: δ = 0.026 mm/s which is in agreement with Rolfe *et al.* [80] who reported an isomer shift value of 0.020±0.06 mm/s for the TiFe phase.

The S1 and S2 spectral components dominates the Mössbauer spectrum with a relative area fraction to 24% and 80% compare to D1 value of 5% and 1% for SL1 components. The line width of the spectrum for the as-milled powder sample was determined as 0.28 mm/s which increased to 0.33 mm/s for the as-sintered sample. This indicates that ^{57}Fe is involved in different bonding mechanisms with surroundings in the sintered sample where it reacts with other elements compared to the milled powder sample.

The hyperfine parameters obtained for FeWC and FeCo correspond to Fe in the 3+ charge state with an electronic configuration $3d^5$. The isomer shift and quadrupole splitting values of δ = 0.026 mm/ and ΔE_Q = 0.54 mm/s suggest that the TiFe phase corresponds to tetravalent Fe^{4+} with a $3d^4$ electronic configuration.

Chapter 5

Conclusions and Recommendations

The aim of the study was to understand how the additional Fe binder affects the properties of the materials under study. To achieve this, the following techniques were applied namely Vickers hardness, scanning electron microscopy (SEM), energy dispersive X-ray spectroscopy (EDS), X-ray diffraction (XRD) and strain analysis in order to understand the structural, electronic, magnetic effects and to identify different phases in the materials.

Two samples WC-Co-TiC and WC-Co-TiC-Fe were prepared by ball milling for 15 hours at a speed of 140 rpm. Thereafter, the samples were sintered at Pilot Tools facility at temperatures ranging from 1000 °C to 1200 °C. In the present work, the Vickers hardness and SEM-EDS were measured on the as-sintered samples, followed by XRD, strain and Mössbauer spectroscopy measurements on the as-milled powder and as-sintered samples.

The second sample WC-Co-TiC-Fe was obtained by the addition of a volume of the binder 20% of Fe to the WC-Co-TiC sample. This resulted in a decrease of the Vickers hardness value from 13316±682 MPa to 8051±403 MPa. The SEM-EDS microstructure results for the as-sintered sample proved that Fe was a major element in the binder phase in the overall spectrum, which decreased the Vickers Hardness value of the sample under study. Iron was preferentially attached to cobalt due to their similar oxidation states and ionic radii.

The XRD results obtained for the as-milled powder sample shows the formation of the CoFe phase after a sufficiently long milling time of 15 hours while transmission Mössbauer spectroscopy was unable to detect this phases. The XRD results for the as-sintered sample shows that Co atoms were incorporated into the Fe lattice resulting in the formation of FeCo phases with bcc crystalline structure, which is in agreement with the results obtained from conversion electron Mössbauer spectroscopy (CEMS) measurements. This is supported by the identification of

these phases through two sextets with magnetic hyperfine values of 35.6 T and 37.2 T which corresponds to FeCo phases observed by other authors [38, 39, 78].

The information obtained through the electric monopole and quadrupole interactions by conversion electron Mössbauer spectroscopy suggests that ^{57}Fe is bonded with tungsten carbide and titanium thus forming FeWC and TiFe phases. The corresponding isomer shift and quadrupole splitting values for D1 and SL1 were found to be $\delta = 0.26$ mm/s, $\Delta E_Q = 0.54$ mm/s and $\delta = 0.026$ mm/s, respectively. The XRD pattern could not reveal the presence of these phases in either the powder or the sintered samples.

The strain result on the as-milled powder and as-sintered WC-Co-TiC samples show that the tungsten carbide phase appears to have little strain, while the titanium carbide phase appears to have no strain. However the cobalt-iron phase appears to have strain associated with it. The strain results for the as-milled powder and sintered WC-Co-TiC-Fe samples revealed that all phases show no strain. It appears as if the crystallites have either reduced their strain during treatment or the average crystallite domain size has increased. This data indicates that a solid state reaction may have occurred. In effect, future efforts should be focused on the stress analysis of the cobalt iron phase collaborate strain results.

It is important to mention that future scope of this work might include:

- Neutron diffraction (ND) studies to evaluate associated stress and strain in the materials under study because ND allows deeper penetration of the sample comparable to XRD.
- Implantation of ^{57}Fe in WC-Co and WC-Co-TiC samples with different fluencies to investigate the effect of Fe concentration and annealing effects.
- Computational investigation to examine the electronic and structural properties of the materials understudy using the code Quantum Espresso.
- A systematic study of the milling process i.e. variation of the grain size of the starting powders and its influence on the hardness of the sintered materials.

Appendices

A. Selection of the Mössbauer peak

The signal from the pre-amplifier is sent to a single channel analyser (SCA) which serves to reject most of the non-resonant background radiation. Generally, three peaks appear on the screen when selecting a SCA before conducting the measurement. In Mössbauer spectroscopy, we are interested in the peak corresponding to 14.4 keV gamma rays as shown in the Figure A1.

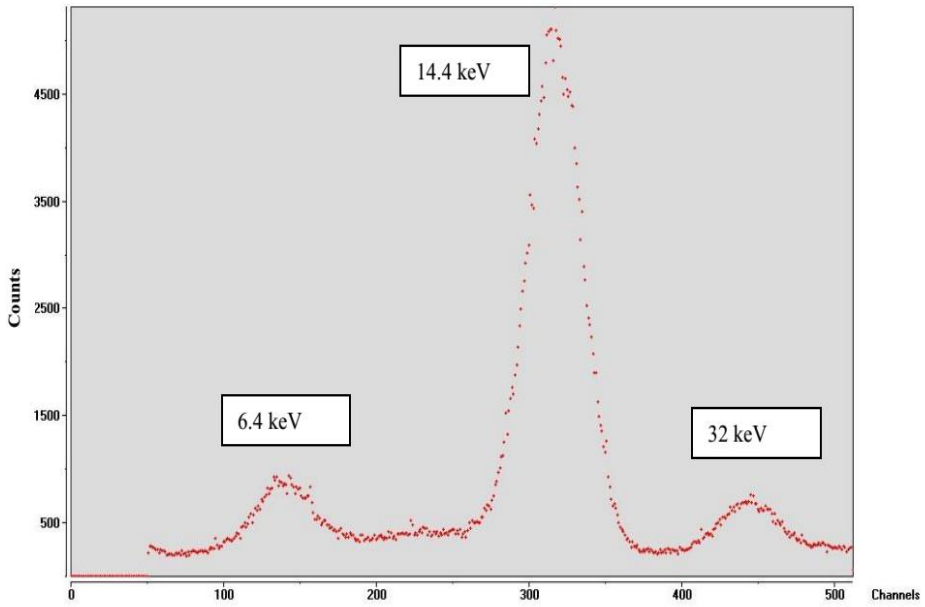

Figure A1: **Pulse height analysis spectrum showing different energies corresponding the gamma and X-ray.**

Selecting a window: After running the measurement in the multi-channel analyser scan mode, the next step is to select a window using the single channel analyser (SCA) mode. The next step is to recommence the measurement in the SCA mode.

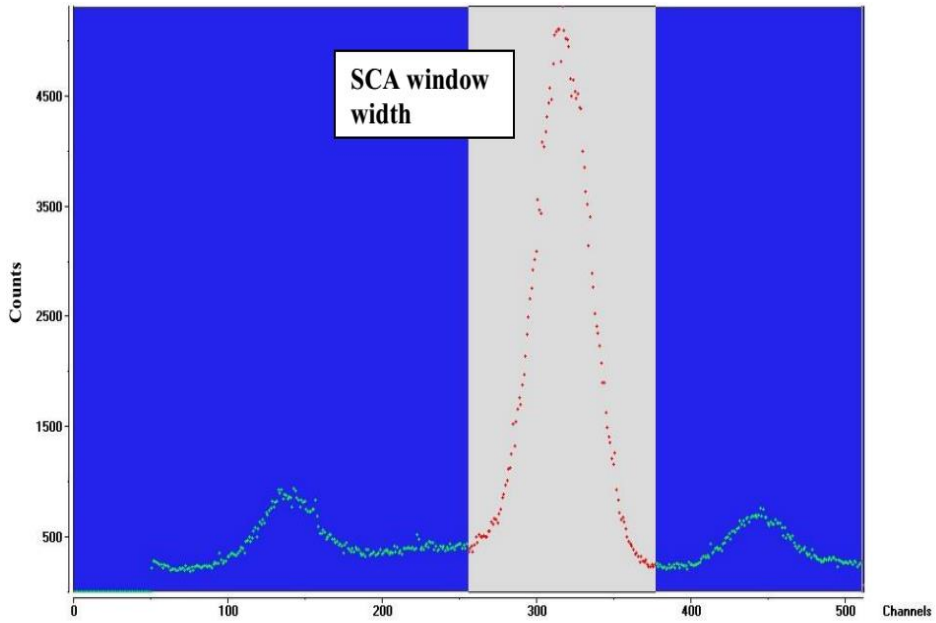

Figure A2: Selecting the SCA window.

B. Vinda fitting of Mössbauer spectra

The as-milled and as-sintered samples were analysed and fitted using a new version of the Code *VindaModels.xlsx* incorporated in Microsoft Excel. The fitting process is summarized as follows:

a. Typical calibration sheet

The typical Vinda tool bar is used for the calibration of the spectra: Insert a cal-sheet followed by loading the spectrum for α-Fe foil which is used as the standard component for the calibration of the system; then the optimization of the chi-square value by changing the folding offset; fold spectrum at which operation is transformation from 1024 to 256 channels; and the last operation is the optimization of the chi-square through the Data-solver menu maintaining constant values for the isomer shift, quadrupole splitting and magnetic hyperfine field. Figure B1 shows the calibration sheet for the data obtained from the TMS measurements on the α-Fe foil.

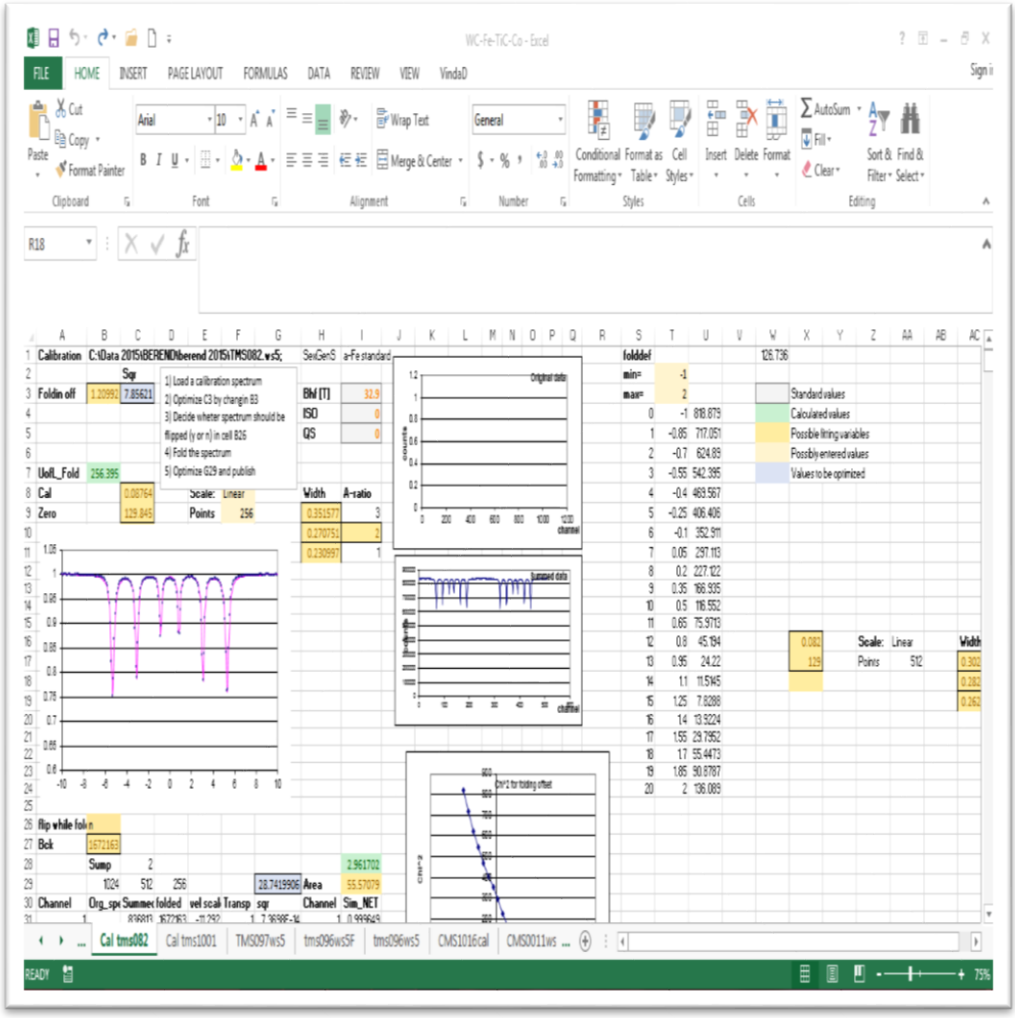

Figure B1: A typical calibration sheet.

b. Single spectrum fitting

The fitting process started with inserting the spec sheet followed by loading the spectrum, the principle of the fitting is based on minimization of the chi-squared (Cell G30) by changing background, area, and all hyperfine parameters in a systematic way. This can be done by selecting all those fitted parameters including line width through the Data-solver parameter. Figure B2 shows the Vinda spec-sheet and explanation of the main fields.

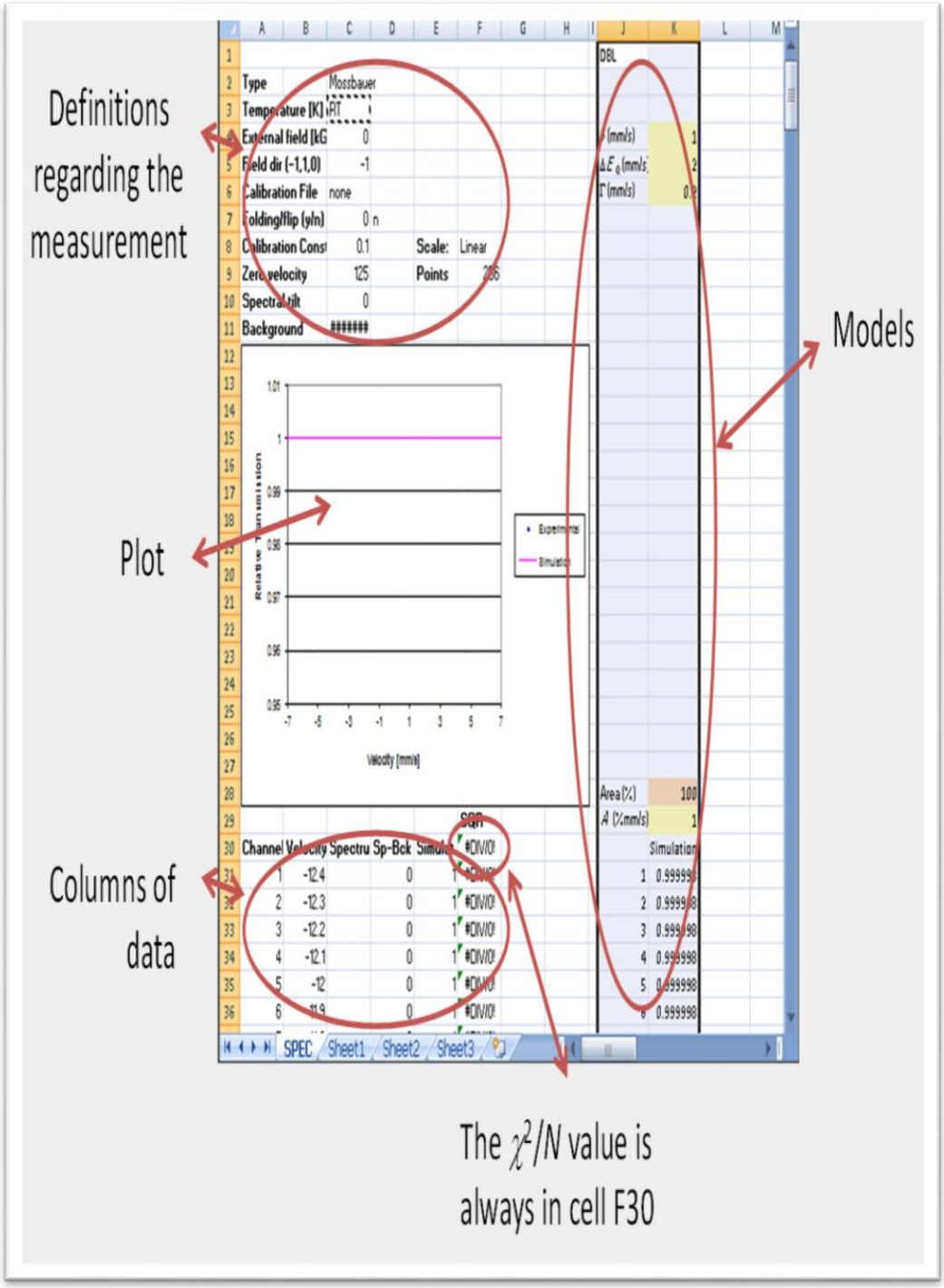

Figure B2: Vinda spec-sheet and explanation of the main field.

The spreadsheet of the single spectrum including the fitted spectral components and fitted parameters are shown in Figure B3.

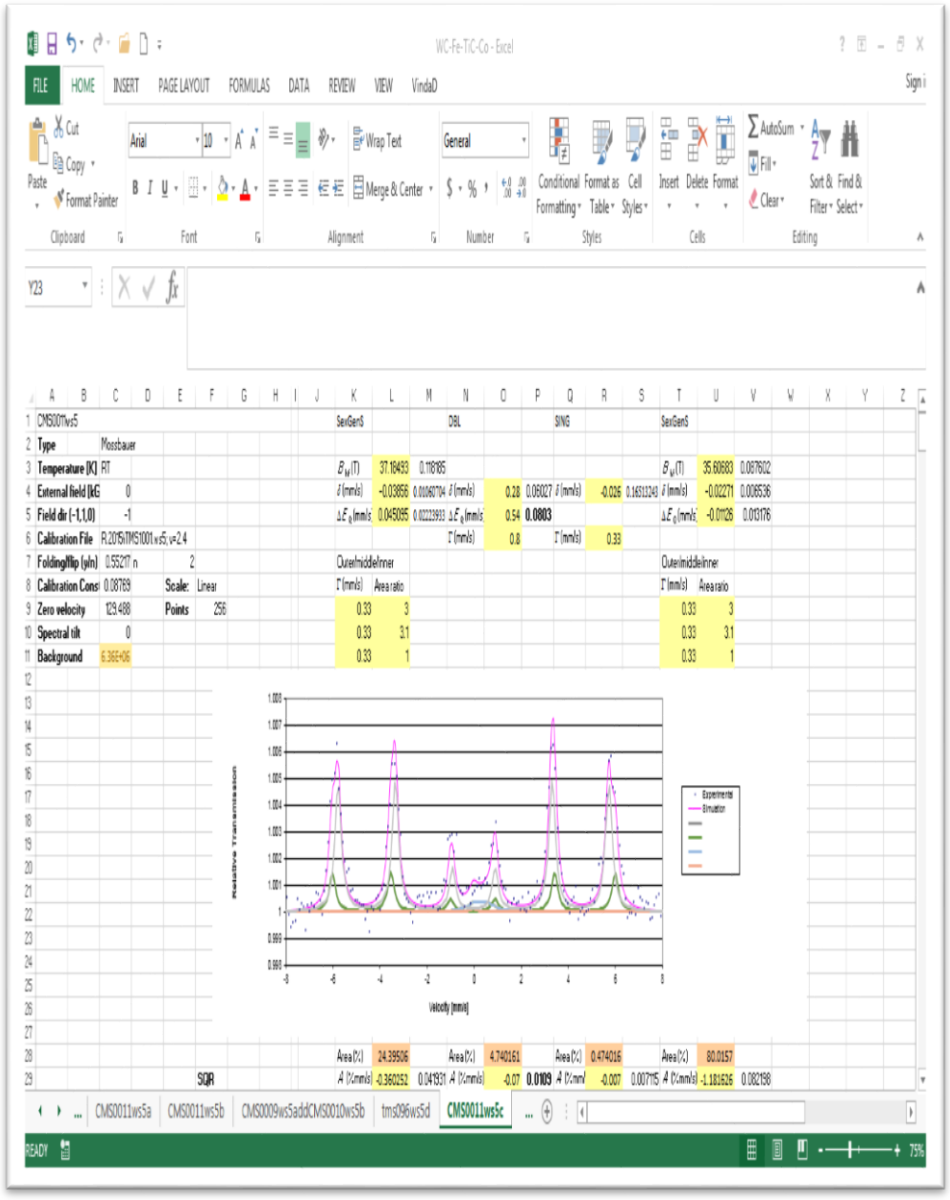

Figure B3: Spreadsheet of a single spectrum with four fitted spectral components.

c. Error analysis

The error values estimated for the fitted parameters have been obtained from the calculation of the Chi-square which is given by

$$\chi^2 = \sum_{i=1}^{N} \frac{(Data_i - Simulation_i)^2}{Data_i}.$$

The value displayed on the worksheets is this value normalized by the number of points. The best fit is found when chi-square approaches 1. Figure B4 shows the error analysis dialog box where F30 is normalized by the number of the data points.

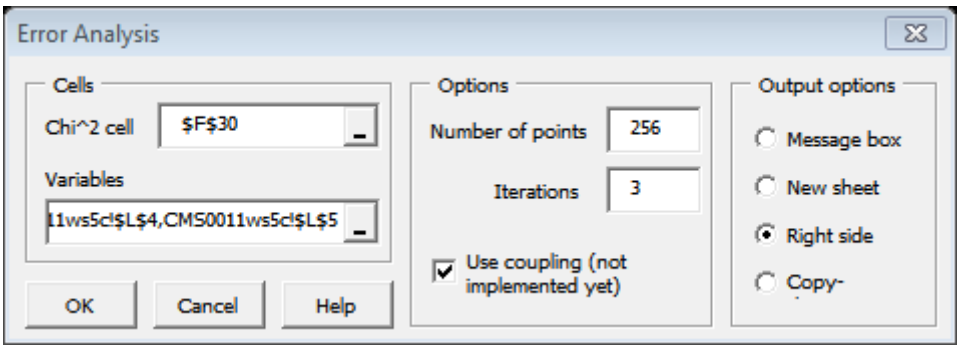

Figure B4: Error analysis dialog box.

The error analysis values are shown for example in columns M, P, S and V in Figure B3.

References

[1] S. Didziulis, and K.B. Bütcher, "A perspective on the properties and surface reactives of carbides and nitrides of titanium and vanadium", *Coord. Chem. Rev*, p. 93-109, 2013.

[2] J.D. Lee, "Concise inorganique chemistry", p. 72-120, 1991.

[3] www.mccallscience.pbworks.com,"Difference between an element, compound and mixture".

[4] www.engineering.toolbox.com, "Modulus of elasticity-Young modulus for some common materials", Engineering Tool Box.

[5] B. Trindade and M.T. Vieira, "Structural characterization of Co-sputtered W-C-Fe films", *Thin Solid Films*, vol. 206, p. 318-322, 1991.

[6] R.L. Sands and C.R. Shakespeare, "Powder metal-particle and application", *Newnws London*, 1966.

[7] V. Mazurovsky, M. Zinigrad, L. Leontiev and V. Lisin, "Material research center" vol. 3, p. 126-133, 2004.

[8] Annual report, "History of tungsten", 2014.

[9] J.D. Knox and J. Gurland, "Tungsten refractor material", *Ref. Mat*, vol. 3, p. 219-228, 1996.

[10] International tungsten industry association report, Itia, 2014.

[11] Z. Yao, J. Jacob *et al.* "Nanograined tungsten carbide-cobalt", *Mat. Modern*, p. 2929, 1996.

[12] P. Oladijo, "Investigation of techniques for determining the residual stress in WC-17Co thermal sprayed coating and studing effect of residual stress on its abrasion resistance", *PhD Thesis Wits University*, 2013.

[13] W. Schedler, "Hard metal for practical", VDI-Verlag, Dusserldof, p. 5-29, 1988.

[14] H.L. De and V. Lovelock, "Powder processing structure relationship in WC-Co thermal spray coating", *Thermal Spray Technology*, vol. 7(3), p. 357-373, 1998.

[15] H. Exner, "Physical and chemical nature of cemented carbide", *International Met. Rev*, vol. 24, p. 149, 1979

[16] M. Graw-Hill Education, "Encyclopedia of science and technology", vol 15, p. 360, 1977.

[17] A.L. Ivanovskii, M.V. Ryzhkov *et al*. "Electronic structure and chemical bonding in crystal and molecular titanium carbide", *Doklady Physical Chemistry*, Vol. 378, p. 1-3 and p. 129-133, 2001.

[18] L. Toth, "Transition metal carbides and nitrides", *Academic Press , New York*, p. 1-6, 1971.

[19] M. Razavi, M.S. Yaghmaee, M.R. Rahimipour, S. Salman and R. Toussi, "Effect of production method on properties of Fe-TiC composite", *Miner Process*, vol. 94, p. 97-100, 2010.

[20] Y. Li, P. Bai, Y. Wang, J. Hu and Z. Guo, "Effect of TiC content on Ni/TiC composites by direct laser fabrication", *Materials & Design*, vol. 30, p. 1409-1412, 2009.

[21] K. Feng, Y. Yang, B. Shen and L. Guo, "In situ synthesis of the TiC/Fe composite by reaction casting", *Materials & Design*, vol. 26, p. 37-40, 2005.

[22] R.P. Pohanish, "Settig's Handbook of Toxic and Hazardous chemical and carcinogenic", *Elsevier,* vol. 6, p. 2670, 2012.

[23] Haynes and M. William, "Handbook of Chemistry and Physics", *CRC Press,* vol. 92, p. 496, 2011.

[24] S.K. Bhaumik, G.S. Upadhayaya and M.L. Validya, "Oxidation behaviour of hard and binder phase modified WC-10Co cemented carbides", *Material Science,* vol. 11, p. 1457-1459, 1992.

[25] G.S. Upadhyaya, "Processing and properties of sintered tool steels and cemented carbides", *Material Science,* vol. 16, p. 465-476, 1993.

[26] J.H. Han and D.Y. Kim, "Determination of three dimensionnal grain size distribution by linear intercept measurement", *Act. Mat.,* vol. 46, p. 2021-2028, 1998.

[27] V.F. Funke, S.I. Yudkovskll and V.S. Panov, "Investigation of the physical properties and structures of TiC-WC-Co alloys", *All-Union Scient. Research Institut of Hard Alloy,* p. 61-66, 1962.

[28] D. Nam, K. Lee and S. Lee "Correlation of microstructure with hardness and wear resistance of carbide-reinforced ferrous surface composites fabricated by High-Energy electron-beam irradiation", *Metallurgical and Materials Transaction,* vol. 39, p. 2626-2634, 2008.

[29] P. Schaaf, G. Rixecker, S. Lee, "Study of nanocrystalline and amorphous powders prepared by mechanical alloying", *Hyperfine Interaction,* vol. 94, p. 2239, 1994.

[30] R. George, "The difficulty of isolating grain boundary components in the Mössbauer spectra of ball-milled materials: Iron and silver-iron alloys", *Solid State,* vol. 122, p. 299-302, 2002.

[31] C. Koch, "Forum 88-90", *Material Science,* p. 243, 1992.

[32] F.L. Zang, C.Y. Wang and M. Zhu, "Nanostructured WC/Co composite powder prepared by high energy ball milling", *Scripta Materia,* vol. 49, p. 1123-1128, 2003.

[33] H. Fecht, *Nanostructures materials,* vol. 6, p. 33, 1995.

[34] P. Matteazzi and G. Le caer, "Room-Temperature mechanosynthesis of carbides by grinding of elemental powders", *Ceramic Society,* vol. 74(6), p. 1382-1390, 1991.

[35] M.H. Staia, E. Ramos, A. Carrasquero, A. Roman *et al.* "Effect of substrate roughness indicated by grit blasting upon adhesion of WC-17Co thermal sprayed coating", *Thin Solid Film,* Vols. 657-664, p. 377-378, 2000.

[36] D. Kin, Y. Choi, Y. Kim, and S. Jumg, "Characteristics of nanophase WC and WC-3wt%(Ni, Co and Fe) alloys using a rapid sintering process for the application of friction stir processing tools", *Materials Science and Engineering* , vol. ID 343619, 2014.

[37] H.K. Park, H.C. Kin, I.K. Ko, and I.J. Shon, *Ceramic International,* vol. 34, p. 1419-1423, 2008.

[38] M. Sorescu and A. Grabias, "Structural and magnetic properties of $Fe_{50}Co_{50}$ system", *Intermetallics,* p. 317-321, 2002.

[39] K. Akkouche, A. Guittoum, N. Boukherroucb and N. Souami, "Evaluation of structure, microstructure and hyperfine properties of nanocrystalline $Fe_{50}Co_{50}$ powders prepared by mechanical alloying", *Magnetism and Magnetic Materials,* vol. 323, p. 2542-2548, 2011.

[40] M. Ncube, "Investigation of the structure and magnetic properties of Ho substituted $BiFeO_3$" *Dissertation Wits University,* 2012.

[41] B.E. Warren, "X-ray Diffraction", p 51-57, 1969.

[42] J.A. Niels, D.M. Morrow and J. Willey, "Elements of modern X-ray physics", *Modern X-ray Physics and New Developments,* p. 173-175, 2001.

[43] R.L. Mössbauer, "Discovery of the Mössbauer Effect", *Hyperfine International* , vol. 126, p. 1-12, 2000.

[44] C.A. Lin and S.T. Lin, *Journal of Physics Condensed Matter*, vol. 5, L247 - L250, 1993.

[45] H. Masenda, "Are Fe and Co implanted ZnO and III-Nitride semiconductors magnetic?", *Thesis Wits University*, 2014.

[46] P. Gütlich and A.Trautwein, "Mössbauer spectroscopy and transition metal chemistry", p. 9-29, 1978.

[47] D. Ping and Y. Chen, "Mössbauer effect in lattice dynamics", Experimental Technique and Applications, *Germany*, p. 17-60, *Wiley-Vch* 2007.

[48] P. Gütlich, Lecture Notes, Univers. of Mainz, " Mössbauer spectroscopy principle and application", p. 37-52, 2007.

[49] Q. Hu, "Mössbauer spectroscopy experiment using ^{57}Fe", *MIT Depart. of Phys*. p. 1-2, 2006

[50] J.M. Cadogan and D.H. Ryan, "Mössbauer spectroscopy", Handbook of Applied Solid State Spectroscopy., *Springer US*, p. 203-220, 2006.

[51] Z. Chai, G. Yuxi and C. Chen, "Nuclear analytical techniques for metallomics and metalloproteomics", *Royal Society of Chemistry*, p. 132-144, 2010.

[52] D.P.E. Dickson and F.J.Berry, "Mössbauer Spectroscopy" *Cambridge Univ. Press,New York*, p. 10-23, 1986.

[53] P. Gütlich, E. Bill and A. Trautwein, "Mössbauer spectroscopy and transition metal chemistry", Fundamental and application, Springer-Verlag, p. 85, 2011.

[54] E. Kuzmann, S. Nagy, and A. Vertes, "Critical review of analytical applications of Mössbauer spectroscopy illustrated by mineralogical and geological examples", *Pure Applied Chemistry*, vol. 75, p. 801-858, 2003.

[55] A.P. Carratta, "NMR-MRI, μSR and Mössbauer spectroscopy in molecular Magnets", *Springer-Verlarg*, p. 227-234, 2007.

[56] G. Weyer, and the ISOLDE, "Mössbauer Spectroscopy at ISOLDE", *Hyperfine Interactions*, vol. 129, p. 371-390, 2000.

[57] K.M. Spiers, D.M. Paganin, and J.D. Cashion, "The effect of vacancy ordering on quadrupole shifts in Mössbauer spectra of Maghemite", *Condensed Matter*, vol. 23, p.2, 2011.

[58] P. Z. Su, *Acta Crystallographia*, Vol. A52748-56, 1996.

[59] K. Brookes, "Hard Metal and other hard materials", *International Carbide Data Hertfordshire*, UK, 1975.

[60] H. Konrad, "Hardness Testing Principles and Application", p. 50-55. 2011.

[61] www.nextgentest.com, "Metals Hardness Testers/Vickers-Hardness-Testers".

[62] A. E92-82, "Standard Test Method for Vickers Hardness of Metallic materials", *ATSM International*, West conshohocken, Reapproved 2003.

[63] Annual report of NFMC spring School, "Fundamentals of scanning electron microscopy and energy dispersive X-ray analysis in SEM and TEM", *University of Belgrade, Serbia*, April 2011.

[64] J. Pina, "Study by X-ray Diffraction and mechanical analysis of residual stress generation during thermal spraying", *Material Science and Engineering*, vol. A347, p. 21-30, 2003.

[65] H.W. Carpenter, R.G. Reid and R. Paskaramoorthy, "Extension of the layer removal technique for the measurement of residual stress in layered anisotopic cylinders", *Mech. Mater,* 2014.

[66] S. Koussios and R.D.B. Sevenois, "Analytical method for stress analysis of two dimension flat anisotopic plates with Notches", *Applied Mechanics Reviews*, 2014.

[67] D. Balzar, N. Audebrand, M.R. Daymond, A. Fitch *et al*. "Size-strain line-broadening analysis of the ceria round-robin sample", *Applied Crystallography,* vol. 37, p. 911-924, 2004.

[68] G. Weyer. Application of Parallel-Plate Avalanche Counters in Mössbauer spectroscopy. in I.J. Gruverman and C.W. Seidel, "Mössbauer effect metholodology", New York and London: Plenum Press, 1976.

[69] M. Darby, D.G. Agresti, M.W.Schacfer, C.A. Grant and E.C. Sklute, "Mössbauer spetroscopy of earth and planetary materials", 2006.

[70] A. Vertes, S. Nagy, Z. Klencsar, G. Lovas and F. Rosch, "Handbook of Nuclear Chemistry", *Springer science+Business,* 2011.

[71] G.J. Long, D. Haulot, Q.A. Pankhrust, D. Vandormael, F. Grandjean, "Mössbauer Effect and X-ray spectral study of sonochemically prepared amorphous iron", *Physical Review B,* vol. 57, p. 17, 1998.

[72] H. Gunnlaugsson, "Spreadsheet Based Analysis of Mössbauer Spectra", *Hyperfine Interaction,* 2015.

[73] N. Brayner, "Evaluation of erosion-corrosion on Ruthenium enriched hardmetal coating", *MSc Dissertation University of Johannesburg*, 2014.

[74] D.J. Varacalle, G.R. Smolik, G.C. Wilson, G. Irons and A. Walter, "An evaluation of tungsten carbide coatings fabricated with the plasma spraying process", *Minerals, Metals and Materials Society,* p. 121-134, 1990.

[75] J.M. Guilemay, J. Nutting and J.M. de Paco, "Characterization of three WC-12Co powders and coatings obtained by high velocity Oxyl-fuel spraying", *Association of Italiana di Metallurgica, Millan,* p. 395-398, 1996.

[76] H.B. Toby, "R-factors in Rietveld analysis: How good is good enough?", *International centre for Diffraction Data*, vol. 21, p. 67-70, 2006.

[77] T.Szumiata, M. Gzik-Szumiata, K. Brzózka *et al.* "Influence of milling and compaction process on magnetic properites of FeCo powder," *Acta Physica Polonica,* vol. 115, p. 1, 2009.

[78] H. Moumeni, S. Alleg and J.M. Greneche, "Structural properties of $Fe_{50}Co_{50}$ nanostructure powder prepared by mechanically alloying", *Alloy and compound,* vol. 386, p. 12-19, 2004.

[79] I.Yu. Petrov and E.A. Shafranovsjy, "Structure and magnetic properties of aerosol nanoparticles of Fe and its alloys", *International Journal Of Inorganic Chemistry,* vol. ID610305, p. 43, 2012.

[80] R.H. Herber, "Chemical Mössbauer spectroscopy", *New York and London,* p. 206, 1984.